ChemPhysMater 5 (2026) 351–365

Contents lists available at ScienceDirect

ChemPhysMater

journal homepage: https://www.keaipublishing.com/en/journals/chemphysmater/

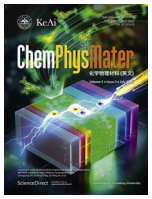

Research Article

Sustainable optoelectronic architecture of polymer-based HTLs for high-performance $CsSnI_2Br$ perovskite solar cells

Wasan J. Kadhem[a], Tariq AlZoubi[b,*], Mahmoud AlGharram[c], Ghaseb Makhadmeh[d], Abdulsalam Abuelsamen[e], Ahmad M. AL-Diabat[f], Jestin Mandumpal[b], Samer H. Zyoud[g]

[a] Department of Scientific Basic Sciences, Faculty of Engineering Technology, Al-Balqa Applied University, Amman 19117, Jordan
[b] College of Engineering and Technology, American University of the Middle East, Egaila 54200, Kuwait
[c] Department of Physics, School of Computing (SC), German Jordanian University, Amman 11180, Jordan
[d] Physics Department, Faculty of Science, Al al-Bayt University, P.O. Box 130040, Mafraq 25113, Jordan
[e] Medical Imaging and Radiography Department, Aqaba University of Technology, Aqaba 77110, Jordan
[f] Department of Physics, Al-Zaytoonah University of Jordan, Amman 11733, Jordan
[g] Nonlinear Dynamics Research Center (NDRC), Department of Mathematics and Sciences, Ajman University, Ajman P.O. Box 346, United Arab Emirates

ARTICLE INFO

Keywords:
Perovskites solar cells
PEDOT:PSS
$CsSnI_2Br$
SCAPS-1D
PSC optoelectronic properties

ABSTRACT

Lead-free cesium tin iodide bromide ($CsSnI_2Br$) perovskite solar cells (PSCs) have emerged as sustainable candidates for next-generation photovoltaics, combining a suitable bandgap with environmental safety. Yet, their performance is hindered by interfacial recombination and the spontaneous oxidation of Sn^{2+} to Sn^{4+}, which degrades carrier mobility and device stability. While chemical stabilization approaches address this oxidation experimentally, its influence on electronic processes can be systematically evaluated through numerical modeling. In this work, the SCAPS-1D simulator was employed to investigate the optoelectronic response of $CsSnI_2Br$ PSCs integrated with different polymer-based hole transport layers (HTLs), namely PEDOT:PSS, Spiro-OMeTAD, PTAA, Poly-TPD, P3HT, and PANI. Key parameters, including HTL thickness, doping concentration, and defect density—were tuned to analyze charge extraction efficiency and minimize interfacial recombination losses. Among the tested configurations, PEDOT:PSS yielded the highest simulated power conversion efficiency of approximately 21.4%, attributed to its favorable band alignment and enhanced hole mobility. Optimal performance was obtained for an absorber thickness of 0.8 μm and HTL thickness in the 50–80 nm range, provided that bulk and interfacial defect densities were below 5×10^{14} and 1×10^{15} cm^{-3}, respectively. Additional improvements were achieved with TiO_2 ETL doping levels of 10^{17}–10^{18} cm^{-3} and a back-contact work function near 4.8 eV. The device maintained robust output up to 320 K, demonstrating stable charge transport and reduced trap-mediated losses. These results provide valuable theoretical insights for optimizing HTL selection and interface engineering in efficient, lead-free perovskite photovoltaics.

1. Introduction

Photovoltaic technologies continue to gain momentum as a clean and viable response to escalating global energy demands. Over the years, a wide range of solar cell architectures has been developed with a core objective of optimizing power conversion efficiency (PCE) while maintaining economic feasibility [1]. Silicon-based devices, although extensively studied due to their abundance and maturity, often face challenges related to production costs and moderate PCE values [2,3]. As a result, attention has progressively shifted toward innovative thin-film alternatives that promise enhanced performance at reduced fabrication expenses. Among these, third-generation solar cells, including dye-sensitized, perovskite, and organic photovoltaic systems have demonstrated significant breakthroughs. Cesium tin iodide bromide ($CsSnI_2Br$), a remarkable and eco-friendly halide perovskite, has recently captured significant attention as a sustainable alternative to conventional lead-based photovoltaic materials, particularly methylammonium lead iodide ($MAPbI_3$), which pose serious health and environmental risks due to their lead content [4,5].

$CsSnI_2Br$ PSC, by contrast, employs tin instead of lead, significantly lowering toxicity without compromising critical optoelectronic characteristics essential for efficient solar energy harvesting. Structurally, $CsSnI_2Br$ crystallizes into a stable three-dimensional framework composed of corner-sharing SnX_6 octahedra and cesium ions, forming robust perovskite lattices that favor strong optical absorption and excellent carrier transport properties [6]. This composition features an optimal

* Corresponding author.
E-mail address: tariq.alzoubi@aum.edu.kw (T. AlZoubi).

https://doi.org/10.1016/j.chphma.2026.03.003
Received 22 January 2026; Received in revised form 3 March 2026; Accepted 9 March 2026
Available online 18 March 2026
2772-5715/© 2026 The Authors. Publishing Services by Elsevier B.V. on behalf of KeAi Communications Co. Ltd. This is an open access article under the CC BY-NC-ND license (http://creativecommons.org/licenses/by-nc-nd/4.0/)

bandgap ranging from approximately 1.3–1.5 eV, closely matching the ideal theoretical limit for single-junction photovoltaics, thereby maximizing efficiency potential [7,8]. Furthermore, the partial substitution of iodide by bromide ions notably enhances both thermal stability and ambient durability, alleviating the critical issue of rapid degradation common to pure tin iodide perovskites, such as $CsSnI_3$ [9,10]. Despite these notable advantages, $CsSnI_2Br$ perovskites still face inherent challenges, especially the oxidation of Sn^{2+} ions to Sn^{4+} in the presence of moisture and oxygen, which adversely affects device stability and performance [11,12]. Current experimental and computational research activities on $CsSnI_2Br$ perovskite materials have intensified significantly, reflecting the material's high potential and growing interest within the photovoltaic community [13]. The ongoing research momentum highlights the enormous potential of $CsSnI_2Br$ perovskite as a sustainable, environmentally friendly, and high-performance material poised to reshape the future landscape of photovoltaic technologies and green energy solutions [14].

Experimentally, recent studies have achieved substantial improvements in solar cell performance, with the current record power conversion efficiency (PCE) reaching approximately 11.9% under optimized laboratory conditions [15]. Researchers have primarily focused on innovative processing techniques, compositional engineering, and interface optimization, employing antioxidant additives (such as SnF_2) and 2D/3D heterostructures to suppress the oxidation of Sn^{2+} and enhance stability and efficiency [16]. Concurrently, advanced computational studies, including density functional theory (DFT) and molecular dynamics simulations, have been instrumental in unveiling deeper insights into the defect chemistry, electronic band structure tuning, charge transport mechanisms, and structural dynamics of $CsSnI_2Br$ [17,18]. Such simulations have guided experiments by predicting optimal compositions, identifying effective doping strategies, and elucidating defect passivation methods that significantly improve device performance and longevity [19]. Together, these comprehensive experimental and theoretical efforts continue to push forward the performance benchmarks of $CsSnI_2Br$-based photovoltaics, moving the PV technology closer to commercial viability and highlighting its significant role in the future of sustainable energy systems [20,21].

Despite significant advancements, $CsSnI_2Br$-based perovskite solar cells still face critical challenges that hinder their widespread adoption, primarily associated with the inherent instability of Sn^{2+} ions against oxidation when exposed to ambient moisture and oxygen [22,23]. This oxidative instability leads to rapid performance degradation, decreased open-circuit voltage, and short operational lifetimes. Moreover, nonradiative recombination due to defect states, grain boundary imperfections, and interface mismatches significantly reduce device efficiency and reliability. To tackle these challenges, recent research efforts have increasingly emphasized integrating advanced polymeric materials as hole transport layers (HTLs). However, their performance is often constrained by Sn^{2+} oxidation, defect formation, and inefficient charge extraction at the perovskite/hole transport layer (HTL) interface. Sn^{2+} oxidation, a significant challenge for tin-based perovskites, leads to the formation of Sn^{4+}, which introduces deep-level trap states within the perovskite layer, drastically reducing charge carrier lifetimes and increasing non-radiative recombination. Polymer-based HTLs can effectively mitigate this issue through several mechanisms [24,25]. Firstly, many conductive polymers, such as PEDOT:PSS and PTAA, exhibit high work functions and favorable energy-level alignments with the valence band of $CsSnI_2Br$, promoting efficient hole extraction and reducing the accumulation of photogenerated holes at the interface, which can otherwise accelerate Sn^{2+} oxidation [14,26,27]. Secondly, the hydrophobic nature of certain polymer HTLs, including PTAA and Poly-TPD, helps form a protective barrier, minimizing moisture ingress, which is a primary driver of Sn^{2+} oxidation [28,29]. Additionally, these polymers can suppress interfacial degradation by providing a smoother, defect-free surface, reducing local electric field intensities that can trigger oxidation. Polymers such as poly(triarylamine) derivatives (e.g., PTAA) and poly(3-hexylthiophene) (P3HT) offer promising solutions, providing effective interfacial passivation, efficient charge extraction, and robust protection against environmental degradation. Polymer HTLs not only suppress tin oxidation by reducing oxygen penetration but also enhance morphological stability, improve interfacial contact, and consequently boost overall photovoltaic performance and device longevity. This strategic integration of polymeric materials with $CsSnI_2Br$ perovskites thus represents a pivotal direction for addressing current challenges, enhancing both efficiency and stability, and accelerating the commercial realization of sustainable, lead-free perovskite solar cells.

A polymeric hole transport layer (HTL) has become critical to improving the efficiency and durability of perovskite solar cells, especially those that use lead-free absorbers such as $CsSnI_2Br$. These materials are not only responsible for extracting photogenerated holes, but they also play a critical role in stabilizing the sensitive perovskite/HTL interface. Among the most studied are PEDOT:PSS, Spiro-OMeTAD, P3HT, poly-TPD, PTAA, and polyaniline (PANI), each with distinct set of advantages. PEDOT:PSS, for instance, is widely used for its ease of processing and favorable work function, but its acidic and hygroscopic nature can compromise device longevity and promote ITO corrosion [30]. Spiro-OMeTAD, the benchmark HTL in high-efficiency PSCs, offers excellent energy-level alignment and hole mobility, but its reliance on hygroscopic dopants like Li-TFSI often accelerates moisture ingress and triggers Sn^{2+} oxidation in tin-based devices. This has shifted attention toward dopant-free polymeric alternatives such as PTAA and poly-TPD, which form uniform, hydrophobic films that suppress nonradiative recombination and moisture penetration, while maintaining efficient charge transport. PTAA passivates trap states and improves interfacial contact, leading to enhanced open-circuit voltages and extended operational lifetimes. Likewise, poly-TPD not only facilitates smoother film formation but also improves crystalline at the perovskite interface, which is essential for reducing charge loss pathways. P3HT, a low-cost, semiconducting polymer, offers excellent thermal and environmental stability, forming hydrophobic layers that protect the underlying perovskite from ambient degradation—even without encapsulation [31]. Meanwhile, PANI stands out as a chemically robust, redox-active HTL capable of dual functionality: it supports charge transport while simultaneously shielding Sn^{2+} ions from oxidative degradation. These polymers go far beyond their electrical role—they actively influence interface chemistry, mechanical integrity, and environmental resilience. Supported by both experimental and simulation studies, their integration has proven to be a key strategy in tackling the fundamental instability challenges of tin-based perovskites, opening pathways to high-efficiency, lead-free solar cells that are both practical and sustainable.

The primary objective of this study is to systematically investigate and optimize the integration of polymeric materials as hole transport layers (HTLs) in $CsSnI_2Br$-based perovskite solar cells by employing the powerful numerical simulation tool, SCAPS-1D. Utilizing SCAPS-1D, a well-established and highly effective photovoltaic simulation software, allows detailed exploration of the influence of polymer HTLs—including materials such as PEDOT:PSS, Spiro-OMeTAD, P3HT, poly-TPD, PTAA, and polyaniline (PANI) on critical device parameters, such as charge carrier dynamics, recombination processes, and energy band alignment at the perovskite/HTL interface [32]. In addition to evaluating HTL performance, this study also explores the optimization of back-contact materials, bulk defect densities, interfacial defect states, and operating temperature effects, all of which significantly influence overall device stability and power conversion efficiency (PCE). Specifically, optimizing the work function of the back contact and minimizing bulk and interface defect densities are critical for reducing recombination losses and maximizing open-circuit voltage. Through rigorous computational modeling, the study aims to identify the optimal polymer HTL candidates, determine ideal thickness and doping levels, and evaluate their capability to effectively mitigate oxidation-induced degradation of Sn^{2+} ions, thus enhancing device stability, efficiency, and overall performance. By providing theoretical insights and clear guidelines for experimental vali-

dation, this approach seeks to accelerate the development and practical realization of stable, efficient, and environmentally friendly $CsSnI_2Br$ solar cells.

2. Model architecture and computational strategy

In this work, SCAPS-1D was adopted as the core simulation platform to explore and optimize the performance of the proposed $CsSnI_2Br$-based perovskite solar cell architecture. The SCAPS-1D platform originates from development efforts carried out by the Electronics and Information Systems division at Ghent University in Belgium. SCAPS-1D has earned widespread recognition for its precision in modeling the complex electrical and optical behavior of multilayer photovoltaic devices [33,34]. Unlike empirical trial-and-error approaches, SCAPS-1D enables a physics-based understanding of device operation by numerically utilizing Poisson's equation and the carrier continuity equations, thus capturing the detailed movement and recombination dynamics of electrons and holes across each layer. Its flexibility makes it suitable for simulating a wide variety of thin-film technologies, including but not limited to perovskites, CZTS, CdTe, CIGS, and crystalline silicon [3,35–42]. One of the tool's most valuable assets is its ability to simulate realistic device behavior that aligns closely with experimental observations, making it ideal for pre-fabrication performance forecasting and materials screening. In addition to calculating current–voltage (J–V) characteristics, SCAPS-1D provides access to critical diagnostics such as energy band diagrams, defect distributions, and external quantum efficiency (EQE) spectra, which collectively offer deep insight into charge extraction, interfacial losses, and spectral response. Through this virtual design environment, the study not only examines how polymeric HTLs influence overall device efficiency but also identifies key interfacial and electronic parameters that govern the photovoltaic response, enabling data-driven strategies for advancing lead-free perovskite technologies.

Beyond its ability to model charge dynamics and energy band alignment, SCAPS-1D provides a robust framework for extracting the key performance indicators that define solar cell operation [43]. Among the key output parameters are the open-circuit voltage (V_{oc}), which denotes the maximum voltage achievable in the absence of current, and the short-circuit current density (J_{sc}), which represents the current produced when the terminals are directly connected without an external bias. The model also extracts the fill factor (FF), a measure of how closely the device approaches its ideal power output, and the power conversion efficiency (PCE), which specifies the proportion of incident solar energy converted into electrical power. All simulations were performed under standard test conditions consisting of a device temperature of 300 K, a radiative flux of 1000 W per square meter, and an air mass of 1.5. These conditions are widely adopted in research community to ensure consistency and comparability in the evaluation of photovoltaic device performance.

These conditions closely replicate midday sunlight on a clear day in mid-latitudes, offering a reliable basis for evaluating and predicting real-world device behavior. By simulating under these controlled parameters, we can not only analyze performance trends with high fidelity but also gain insight into the interplay of materials, interfaces, and architecture in determining device efficiency. This modeling approach enables a data-driven path toward fine-tuning solar cell designs and guiding future experimental efforts with greater precision and confidence.

This study is centered on optimizing the photovoltaic performance of a $CsSnI_2Br$-based perovskite solar cell architecture by incorporating various polymeric hole transport layers (HTLs) and evaluating their impact using the SCAPS-1D simulation environment. The reference device configuration, Ag/Polymer (HTLs)/$CsSnI_2Br$/TiO_2/FTO, was selected based on its relevance to lead-free, stable device architecturesAn absorber thickness of 400 nm was used as the baseline for all comparative simulations (Fig. 1). A systematic parametric sweep was conducted, varying key physical and electronic parameters such as absorber thickness, ETL thickness, doping levels, interface defect densities, bias voltages, and operating temperatures to understand their influence on critical output metrics including V_{oc}, J_{sc}, FF, and PCE. The study also explored the integration of several polymer-based HTLs namely PEDOT:PSS, Spiro-OMeTAD, PTAA, poly-TPD, P3HT, and PANI and their influence on hole transport efficiency, energy-level alignment, and interfacial recombination suppression. Tables 1 and 2 summarize the intrinsic material parameters and interface defect characteristics employed in the simulations to ensure accurate modeling of interfacial charge dynamics. Through this multi-variable optimization, the study offers predictive insights into the interplay between material properties and device architecture, enabling the identification of conditions that maximize power conversion efficiency while enhancing long-term stability. These findings contribute to the growing effort to develop environmentally benign, high-performance perovskite solar cells based on tin halide absorbers and scalable, dopant-free transport layers. Photocurrent generation in the simulated $CsSnI_2Br$-based device begins when incident photons with energy equal to or greater than the absorber's bandgap generate electron–hole pairs. These carriers are then separated and driven by the built-in electric field at the HTL/perovskite and ETL/perovskite interfaces, with holes migrating toward the HTL and electrons toward the ETL. This process initiates current flow, governed by both drift and diffusion mechanisms, and forms the basis of device operation under illumination.

The optimization strategy employed in this study follows a sequential layer-by-layer approach under standard test conditions (AM 1.5G illumination, 100 mW cm^{-2} incident power density, and 300 K temperature). Each device parameter (HTL thickness, absorber thickness, ETL doping concentration, back-contact work function, bulk defect density, and interface defect density) was first independently optimized while keeping all other parameters fixed at the baseline reference values listed

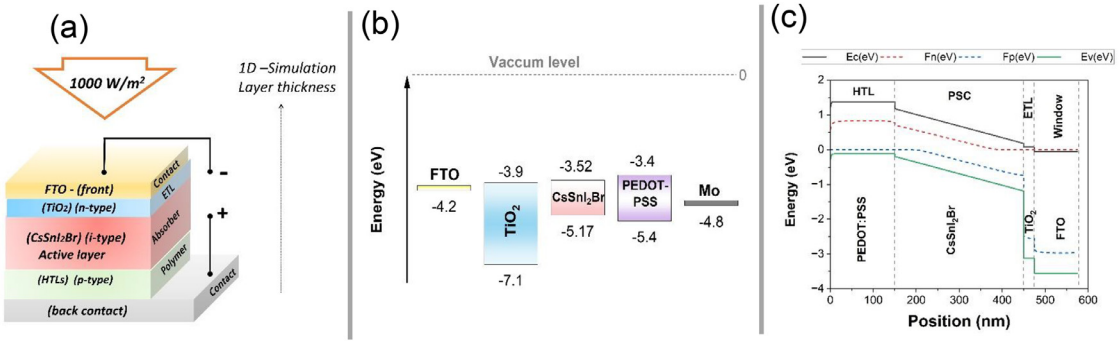

Fig. 1. Schematic diagram of the proposed solar cell configuration based on Mo/PEDOT:PSS/ $CsSnI_2Br$//TiO_2/FTO device architecture. (a) Outlines the multilayer architecture. (b) visualizes the interfacial band configuration. (c) captures the positional shifts in the conduction and valence bands, Fermi energy for electron and hole and energy band gaps, as a function of position.

Table 1
A summary of the material and electronic parameters used in the reference simulation at 300 K [19,44–47].

Parameters	ETL (TiO_2)	Absorber ($CsSnI_2Br$)	Applied Polymers as HTLs					
			PEDOT: PSS	Spiro-OMAD	P_3HT	PolyTBD	PTTA	PANI
Thickness (μm)	0.025*	0.8*	0.15*	0.15	0.15	0.15	0.15	0.15
Bandgap (eV)	3.2	1.37	1.6	3	1.05	2.9	3.2	2.46
Electron affinity (eV)	3.9	3.8	3.4	2.2	3.9	2.05	2.05	2.15
Dielectric permittivity	9	5.27	3	3.2	10	3	3.4	3
CB effective DOS (cm^{-3})	2.2×10^{19}	1×10^{19}	2.2×10^{18}	2.2×10^{18}	1×10^{20}	2.8×10^{19}	2.8×10^{19}	2.8×10^{19}
VB effective DOS (cm^{-3})	1.8×10^{19}	1.8×10^{19}	1.8×10^{19}	1.7×10^{19}	1×10^{20}	1×10^{19}	1×10^{19}	1×10^{19}
Electron mobility ($cm^2/(V{\cdot}s)$)	20	2	0.045	2×10^{-4}	0.0018	0.0001	1×10^{-4}	1×10^{-4}
Hole mobility ($cm^2/(V{\cdot}s)$)	10	1	0.045	2.16×10^{-4}	0.0186	0.0001	5×10^{-4}	2.7×10^{-5}
Donor density N_D (cm^{-3})	1×10^{18}*	1×10^{13}	0	0	0	0	0	0
Acceptor density N_A (cm^{-3})	0	1×10^{13}	1×10^{18}	1×10^{19}	1×10^{18}	1×10^{18}	1×10^{18}	1×10^{18}
Defect type	SA	Neutral	Neutral	Neutral	Neutral	SA	Neutral	SA
Energetic distribution	Single	Gaussian	Gaussian	Gaussian	Gaussian	Gaussian	Gaussian	Single
Defect density (cm^{-3})	1×10^{14}	1×10^{14}	1×10^{14}*	1×10^{15}	1×10^{13}	1×10^{14}	1×10^{14}	1×10^{14}

* Variable field.

Table 2
Defect parameters assigned to the HTL and ETL interfaces.

Parameters	HTL/$CsSnI_2Br$ interface	$CsSnI_2Br$/ETL interface
Defect type	Donor	Neutral
Capture cross section of electrons (cm^2)	1×10^{-19}	1×10^{-19}
Capture cross section of holes (cm^2)	1×10^{-19}	1×10^{-19}
Reference for the defect energy level E_t	Above E_v	Above E
Energy with respect to reference (eV)	0.6	0.6
Total density (cm^{-2})	1×10^{14}	1×10^{14}*

* Variable field.

in Tables 1 and 2. The optimized value obtained at each stage was then used as the updated baseline configuration for the subsequent parameter sweep. This sequential refinement ensures physical consistency and progressive device improvement while maintaining strict single-variable variation during each individual sweep, thereby avoiding simultaneous parameter coupling.

3. Results and discussion

3.1. Impact of the applied HTL-polymers on the $CsSnI_2Br$-PSC performance

The study was initiated to investigate the impact of the hole transport layer on the performance of formamidinium tin iodide perovskite solar cells PSC. Fig. 2 presents a comparative simulation study of six polymer-based hole transport layers (HTLs)—Spiro-OMeTAD, PEDOT:PSS, PTAA, PolyTBD, P3HT, and PANI—integrated into a $CsSnI_2Br$-based perovskite solar cell structure employing TiO_2 serving as the layer responsible for electron extraction. The current density–voltage response shown in Fig. 2(a) clearly indicates that PEDOT:PSS produces the largest short-circuit current among the evaluated configurations ($J_{sc} \approx 25.4$ mA/cm^2), followed closely by PTAA and PolyTBD with J_{sc} values around 24.5 mA/cm^2. Spiro-OMeTaAD performed moderately well, while P3HT and PANI exhibited significantly lower J_{sc} values, below 18 mA/cm^2. This trend suggests that PEDOT:PSS, PTAA, and PolyTBD offer superior hole extraction and interfacial compatibility with the $CsSnI_2Br$ absorber, likely due to favorable valence band alignment and reduced series resistance. In contrast, P3HT and PANI perform poorly indicative of inefficient carrier transport. This is possibly exacerbated by mismatched energy levels and increased trap-assisted recombination at the interface.

The external quantum efficiency (EQE) spectra in Fig. 2(b) support these findings, as PEDOT:PSS, PTAA, and Spiro-OMeTAD exhibit high and broadband spectral responses, maintaining quantum efficiencies above 85% across the visible region (400–800 nm). This implies efficient photogeneration and collection of charge carriers in these configurations. Conversely, P3HT and PANI show pronounced spectral losses, especially in the 600–800 nm range, which can be attributed to suboptimal film morphology or increased optical losses at the interface due to poor material compatibility with the perovskite layer [48].

The radar plot in Fig. 2(c) offers a multi-metric assessment based on open-circuit voltage (V_{oc}), short-circuit current density (J_{sc}), fill factor (FF), and power conversion efficiency (PCE). PEDOT:PSS and PTAA present the most balanced performance across all parameters. Spiro-OMeTAD reaches the highest V_{oc} (approximately 0.92 V) but suffers from a relatively low FF (~75%), likely due to its dependence on dopants such as Li-TFSI, which can induce instability and recombination losses. P3HT and PANI are clearly disadvantaged, with both low V_{oc} and FF, indicative of non-ideal energy level alignment and higher interfacial resistance.

Fig. 2(d) illustrates the resulting PCE as a function of the HTL material. PEDOT:PSS achieves the highest efficiency at 20.10%, followed by PTAA (18.40%), PolyTBD (18.17%), and Spiro-OMeTAD (17.66%). P3HT records a nominally high PCE of 19.00%, which appears inflated by its elevated J_{sc}; however, its poor EQE response and fill factor suggest that this performance may not be sustainable in practical conditions. PANI shows a substantial drop in PCE to just 4.45%, confirming its unsuitability as an HTL in this architecture.

The observed performance hierarchy can be scientifically attributed to differences in hole mobility, energy level alignment with $CsSnI_2Br$, film morphology, and the ability of each polymer to form low-defect, passivated interfaces. PEDOT:PSS combines optimal energy alignment, high electrical conductivity, and uniform film formation, facilitating efficient charge extraction and minimal interfacial recombination. PTAA and PolyTBD follow similar principles with slightly lower conductivity but improved hydrophobicity, which enhances stability. On the other hand, P3HT and PANI, while structurally robust, suffer from lower hole mobility and suboptimal energetic compatibility. This leads to losses of recombination and reduces photovoltaic output. These findings emphasize the critical role of HTL selection in optimizing lead-free perovskite solar cells' efficiency and stability.

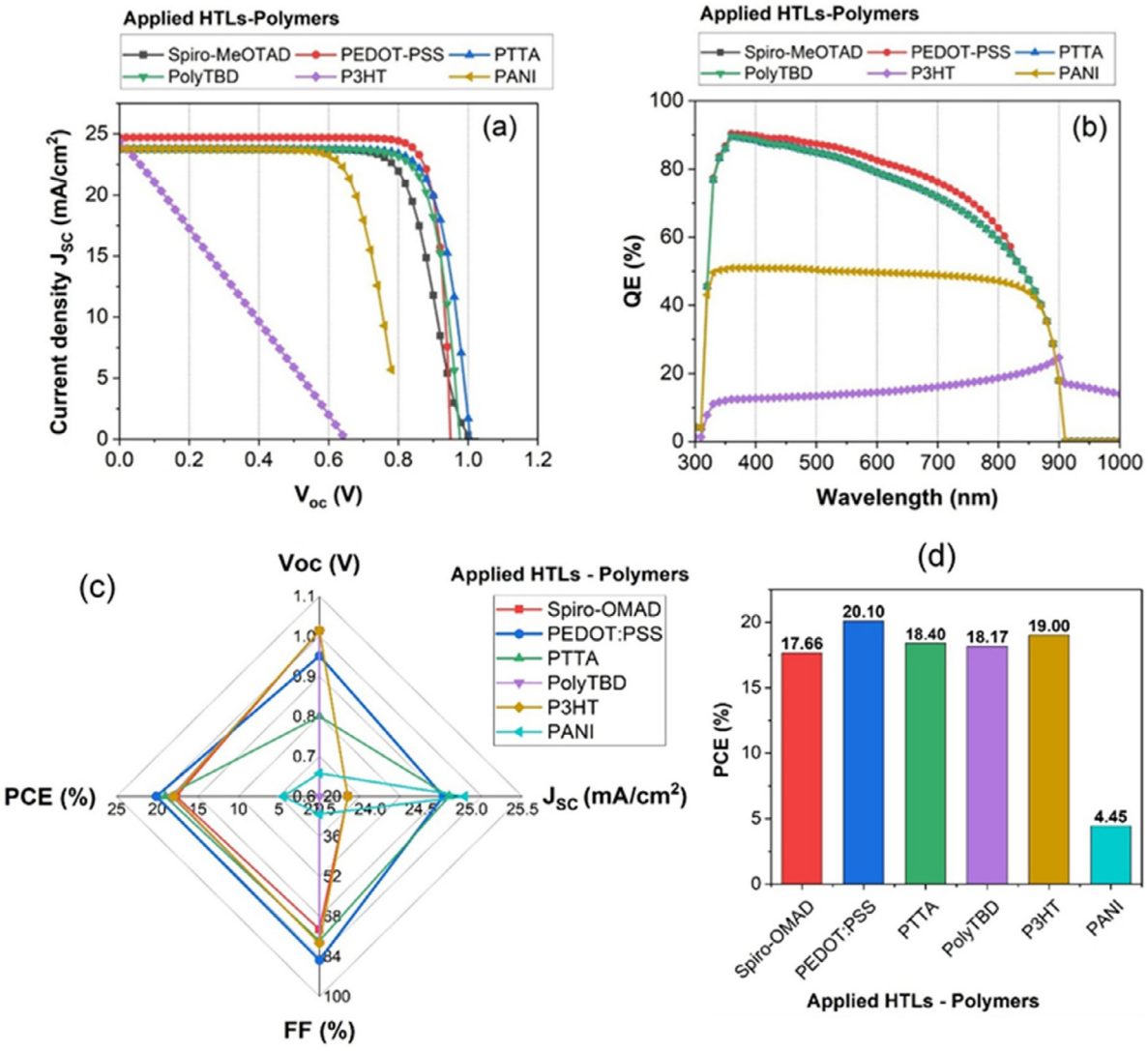

Fig. 2. Simulated photovoltaic response of $CsSnI_2Br$ solar cells employing various polymer-based hole-transport layers, including Spiro-OMeTAD, PEDOT:PSS, PTAA, PolyTBD, P3HT, and PANI. (a) Current density–voltage (*J–V*) characteristics. (b) External quantum efficiency (EQE) spectra illustrating photon-to-electron conversion across the 300–1000 nm range. (c) Radar plot comparing V_{oc}, J_{sc}, fill factor (FF), and power conversion efficiency (PCE). (d) Bar chart showing PCE (%) identifying PEDOT: PSS as the top-performing material with 20.10% efficiency. Practical factors such as film non-uniformity, dopant instability in Spiro-OMeTAD (e.g., Li-TFSI/tBP), hygroscopic degradation, and interfacial corrosion are not neglected; rather, they are represented through their dominant electrical consequences. In drift–diffusion physics, such effects translate into reduced hole mobility and increased bulk/interface trap density, leading to enhanced SRH recombination. The systematic mobility and defect-density sensitivity analyses in Sections 3.3–3.7 show that efficiency collapses beyond bulk Nt ≈ 10^{15} cm^{-3} (Fig. 5) and interface Nt ≈ 5×10^{13} cm^{-2} (Fig. 8), indicating that the reported 21.45% PCE is a defect- and transport-constrained electronic upper bound rather than an assumption of ideal chemical or morphological stability.

3.2. Thickness-dependent correlation and optoelectronic optimization of PEDOT:PSS (HTL) and $CsSnI_2Br$ (absorber)

To systematically evaluate the interdependent effects of the hole transport layer (HTL) and absorber layer thicknesses on device performance, a comprehensive two-parameter optimization study was conducted using SCAPS-1D. In this subsection, the HTL thickness was varied while all other device parameters were fixed at the baseline values defined in Tables 1 and 2 under standard test conditions. The PEDOT:PSS HTL thickness (d_{HTL}) was varied from 0.05 to 0.50 μm, while the $CsSnI_2Br$ perovskite absorber thickness (d_{abs}) spanned 0.2 to 2.0 μm.

As depicted in Fig. 3(b), the open-circuit voltage V_{oc} is governed by the Shockley diode law (Eq. (1)) [49]:

$$V_{oc} = \frac{k_B T}{q} \ln\left(\frac{J_{sc}}{J_0} + 1\right), \quad (1)$$

where J_0 is the reverse saturation current. V_{oc} shows a modest decline with increasing absorber thickness, primarily due to enhanced bulk recombination that elevates J_0. Interestingly, V_{oc} remains nearly invariant with changes in d_{HTL}, indicating that HTL does not introduce significant interfacial recombination within the simulated range. As the absorber becomes thicker, photogeneration (and hence J_{sc}) initially improves, but this is eventually offset by an increase in J_0, primarily due to enhanced bulk recombination. This trade-off ultimately limits open-circuit voltage at larger absorber thicknesses. Thus, optimizing the absorber thickness is crucial to balancing photogeneration and recombination, maximizing the overall efficiency of the photovoltaic device. Additionally, the slight maximum in V_{oc} observed around d_{abs} ≈ 0.4–0.6 μm corresponds to the regime where light absorption is efficient, but recombination losses are still minimal. This region coincides with the early rise in J_{sc} (Fig. 3(c)) without yet triggering substantial recombination-related J_0 penalties. Accordingly, this condition offers an optimum operating point where

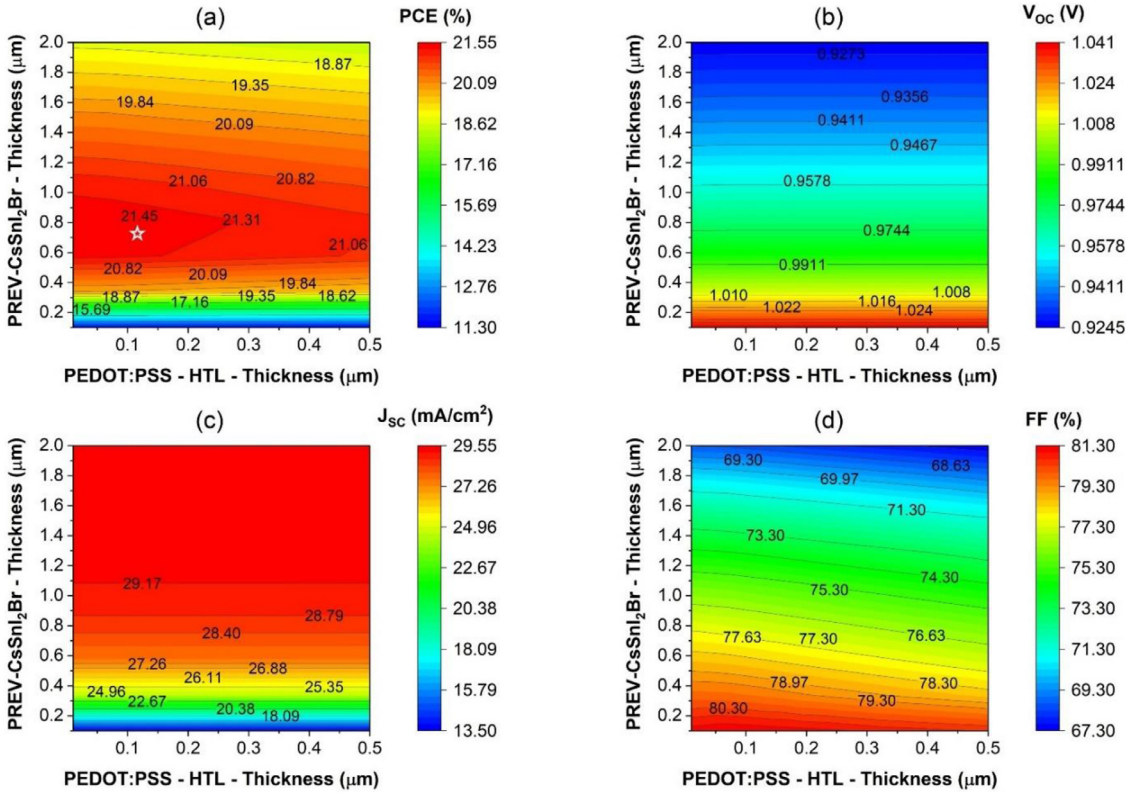

Fig. 3. Simulated contour color map showing the effect of PEDOT: PSS HTL thickness (d_{HTL}) and $CsSnI_2Br$ absorber thickness (d_{abs}) on device performance parameters: (a) PCE, (b) V_{oc}, (c) J_{sc}, and (d) FF. The global optimum (21.45%) occurs at $d_{HTL} \approx 0.05$ μm and $d_{abs} \approx 0.8$ μm, where optical absorption, carrier transport, and resistive losses are optimally balanced.

the voltage is enhanced without diminishing the other key performance parameters.

The short-circuit current density J_{sc}, shown in Fig. 3(c), exhibits a strong positive correlation with absorber thickness, following the integrated Beer–Lambert law (Eq. (2)):

$$J_{sc} = q \int_0^{d_{abs}} \int_{\lambda} \alpha(\lambda)\Phi(\lambda)e^{-\alpha(\lambda)x} d\lambda dx, \quad (2)$$

where, $\Phi(\lambda)$ is the incident photon flux density at λ wavelength, $\alpha(\lambda)$ is Absorption coefficient, and $e^{-\alpha(\lambda)x}$ is the exponential attenuation term, representing how light intensity decreases with depth. he most pronounced trend in Fig. 3(c) is the strong positive correlation between J_{sc} and absorber thickness d_{abs} up to approximately 0.8–1.0 μm. This behavior stems from the wavelength-dependent nature of $\alpha(\lambda)$: higher-energy (shorter-wavelength) photons are absorbed near the surface, while lower-energy (longer-wavelength) photons penetrate deeper into the film.

As d_{abs} increase the device captures more of the long-wavelength photons that would otherwise be transmitted, resulting in increased overall photogeneration and, consequently, higher J_{sc}. This regime is dominated by optical enhancement and matches well with the absorption edge of $CsSnI_2Br$, which has a bandgap of ~1.3–1.4 eV.

However, beyond ~1.0–1.2 μm, the curve begins to saturate and further increases in thickness no longer yield significant gains in J_{sc}. This plateau arises because nearly all photons with energies above the bandgap are already absorbed, and additional thickness adds minimal optical benefit. In fact, deeper photogeneration may occur beyond the minority carrier diffusion length, leading to recombination losses in real devices, though SCAPS idealizations may partially suppress this effect. The combined trends in Fig. 3(c) illustrate that maximizing J_{sc} requires a carefully tuned absorber thickness—thick enough to absorb across the solar spectrum but not so thick that carrier extraction becomes limited. Simultaneously, the HTL should be ultra-thin (20–70 nm) to minimize optical losses and resistive barriers without sacrificing interfacial uniformity or continuity.

These findings align with experimental reports showing that for low-mobility, solution-processed HTLs like PEDOT:PSS, thicknesses beyond ~100 nm introduce resistive and optical penalties. Moreover, in tin-based perovskites like $CsSnI_2Br$—which already suffer from high background carrier concentrations and short carrier lifetimes—minimizing any additional loss mechanisms becomes critical for achieving high J_{sc} and overall efficiency. Fig. 3(d) reveals an important trade-off inherent to photovoltaic device design: increasing absorber thickness improves J_{sc} (as shown in Fig. 3(c)), but at the cost of reducing FF due to increased recombination and transport resistance. This reinforces the concept of an optimal absorber thickness window (~0.8–1.0 μm), beyond which performance gains in current are outweighed by losses in voltage and FF. Similarly, the PEDOT:PSS HTL should be as thin as possible (~50–80 nm) to ensure low resistive losses and efficient hole extraction, without compromising film continuity or interfacial integrity. Extremely thin HTLs (<30 nm) could lead to shunting or poor coverage, while thicker ones add parasitic resistance without benefit. The optimized HTL thickness (0.05 μm) was fixed as the reference value for all subsequent simulations. Likewise, the optimized absorber thickness (0.8 μm) was adopted as the baseline configuration for the subsequent parametric analyses.

3.3. Impact of TiO_2 ETL doping and thickness on HTL-polymer based $CsSnI_2Br$ performance

Fig. 4 presents a comprehensive two-dimensional simulation study evaluating the influence of TiO_2 electron transport layer (ETL) thickness (0.05–2.0 μm) and doping concentration (10^{12}–10^{19} cm^{-3}) on the

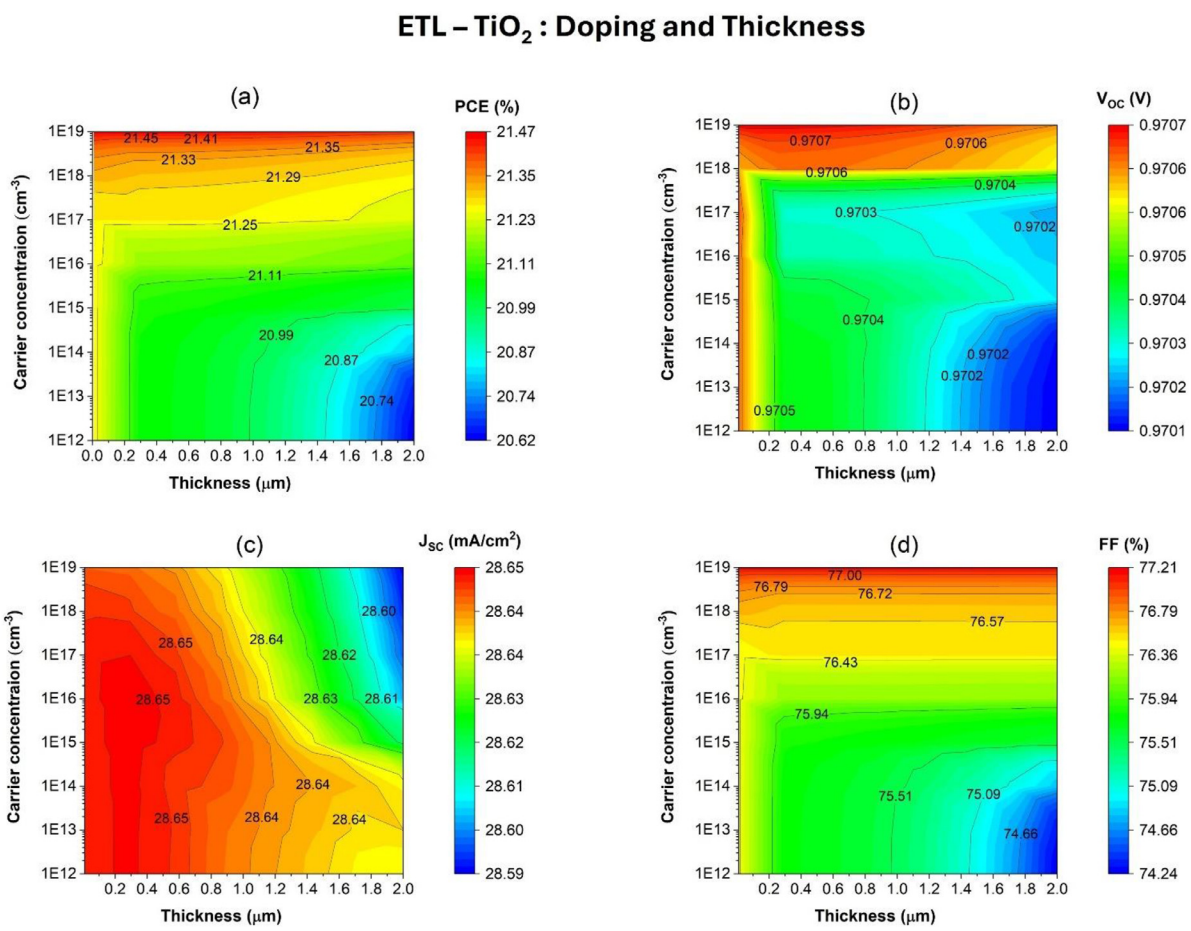

Fig. 4. Contour color maps showing the effects of TiO_2 ETL thickness (0.05–2.0 μm) and doping concentration (10^{12}–10^{19} cm^{-3}) on HTL-Polymer based PV performance: (a) PCE, (b) V_{oc}, (c) J_{sc}, and (d) FF. Optimal efficiency (>21.4%) occurs at high doping (≥10^{17} cm^{-3}) and thin ETL (<0.25 μm), driven by reduced series resistance and suppressed interfacial recombination.

photovoltaic performance of a planar perovskite solar cell. The four subfigures illustrate the variations in (a) power conversion efficiency (PCE), (b) open-circuit voltage (V_{oc}), (c) short-circuit current density (J_{sc}), and (d) fill factor (FF), offering a multidimensional perspective on the optimization of ETL parameters for maximum device efficiency.

With HTL thickness fixed at 0.05 μm and absorber thickness fixed at 0.8 μm, the ETL donor concentration was varied independently to evaluate its influence on device performance.

In Fig. 4(a), the PCE is strongly influenced by both ETL doping and thickness. Peak efficiencies (>21.4%) are achieved at high doping concentrations (≥10^{17} cm^{-3}) and thin TiO_2 layers (<0.2 μm). This enhancement is attributed to reduced series resistance and improved band bending at the perovskite/ETL interface, which collectively improve electron extraction and suppress interfacial recombination. For ETL thicknesses beyond ~0.5 μm, a gradual decline in PCE is observed due to increased bulk resistance and photon losses in the ETL.

Fig. 4(b) reveals that V_{oc} exhibits a slight upward trend with increasing doping concentration, plateauing near 0.9707 V at dopant levels above 10^{17} cm^{-3}. This behavior is governed by the Shockley diode relationship (Eq. (1)). Here, higher doping concentrations reduce the reverse saturation current density J_0, thereby boosting V_{oc}. However, once sufficient interface passivation and electric field strength are achieved, additional doping yields diminishing returns. The influence of ETL thickness on V_{oc} is minimal, suggesting that recombination is predominantly controlled by electronic properties rather than geometrical factors. In Fig. 4(c), the J_{sc} remains relatively stable (~28.59 to 28.65 mA/cm^2) across the entire parameter space. This indicates that variations in ETL doping, and thickness have a limited effect on optical absorption, as the bulk of photogeneration occurs within the perovskite layer. Slight declines in J_{sc} at low doping levels may arise from inefficient electron collection and increased interfacial loss due to poor band alignment or low conductivity in the ETL.

Fig. 4(d) shows that FF is highly sensitive to doping concentration. As doping increases from 10^{12} to 10^{19} cm^{-3}, FF improves from ~74.2% to ~77.2%. This trend results from a significant reduction in series resistance within ETL, which facilitates more efficient charge extraction. The FF is also weakly dependent on ETL thickness; thicker TiO_2 layers (>1 μm) introduce transport-related resistive losses, slightly reducing FF due to prolonged carrier transit times and potential space-charge buildup. Overall, these results suggest that optimal ETL performance is achieved with a doping concentration in the range of 10^{17}–10^{18} cm^{-3} and a TiO_2 thickness between 0.05 and 0.25 μm, which jointly minimize recombination and resistive losses while maintaining effective carrier extraction. These findings align well with experimental design rules for high-efficiency, planar heterojunction perovskite solar cells utilizing compact metal oxide transport layers. The optimal ETL doping concentration of 1×10^{18} cm^{-3} and thickness of 0.5 μm were then fixed for all subsequent simulations.

3.4. Influence of bulk defect density on HTL-polymer based PSC performance

Fig. 5 illustrates the simulated impact of bulk defect density (Nt) on the photovoltaic performance of a planar perovskite solar cell (Table 1).

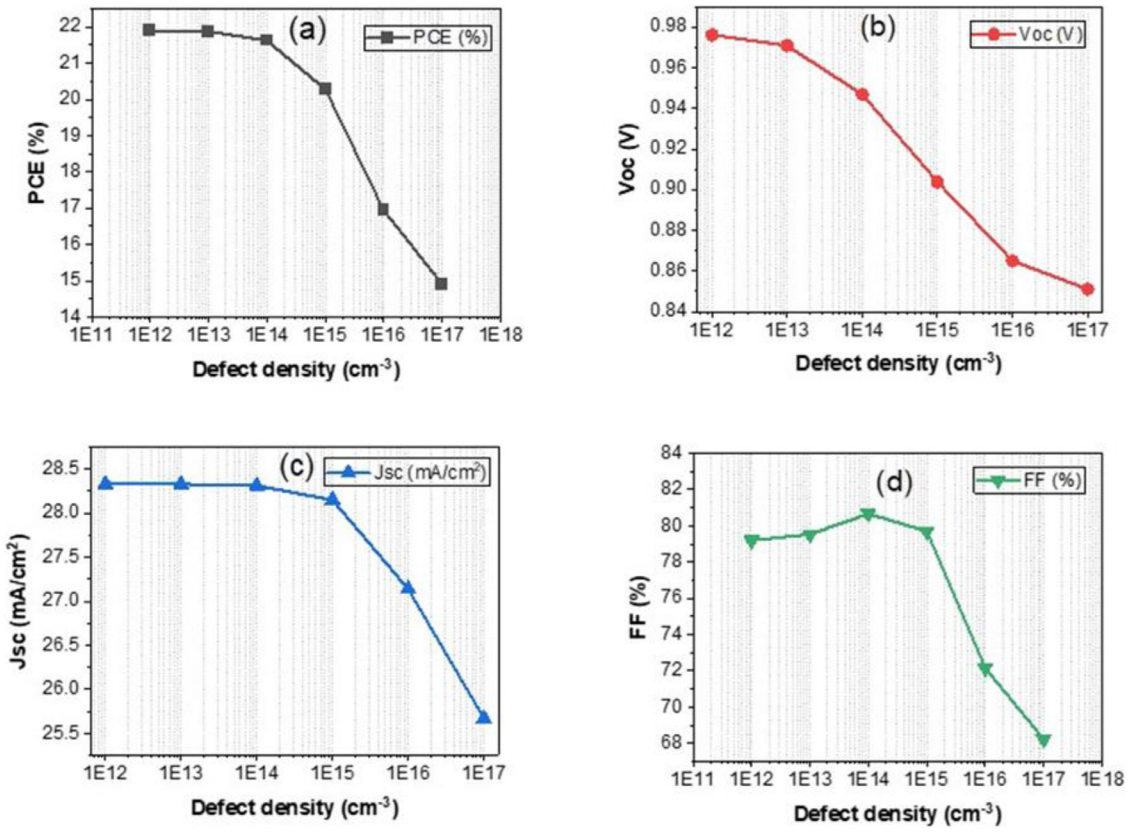

Fig. 5. Impact of bulk defect density (Nt = 10^{12}–10^{17} cm^{-3}) on the photovoltaic performance of a planar HTL-Polymer based PSC, illustrating trends in (a) PCE, (b) V_{oc}, (c) J_{sc}, and (d) FF.

The defect density was varied across several orders of magnitude, from 10^{12} to 10^{17} cm^{-3}, to capture the transition from near-ideal to severely trap-limited regimes. The photovoltaic parameters are evaluated in this section. Under the fully optimized structural and contact configuration in the last section, the bulk defect density in the absorber layer was varied independently to assess recombination sensitivity.

In Fig. 5(a), the PCE shows a gradual decline at low defect densities, followed by a sharp drop beyond Nt~10^{15} cm^{-3}. This behavior reflects the increasing dominance of non-radiative recombination within the bulk perovskite layer. At low Nt, the device operates near the radiative limit, and carriers are efficiently collected. However, as defect density increases, recombination within the depletion and quasi-neutral regions rises substantially, reducing carrier lifetime (τ) and thus photocurrent extraction and voltage generation, leading to a severe reduction in power output. Fig. 4(b) shows a continuous and steep decline in V_{oc} with increasing defect density, dropping from 0.98 V to approximately 0.85 V. According to Eq. (1), As Nt increases, recombination in the bulk raises J_0, directly lowering V_{oc}. The relationship is logarithmic, so even small changes in trap density can produce substantial voltage losses, particularly beyond 10^{14} cm^{-3}. In Fig. 5(c), J_{sc} remains nearly constant (~28.5 mA/cm^2) at low defect densities but declines rapidly for Nt ≥ 10^{15} cm^{-3}. This behavior is attributed to the loss of photogenerated carriers via recombination before they reach the contact interfaces. At high defect densities, the effective carrier diffusion length $L = \sqrt{D\tau}$ decreases significantly, limiting the probability of collection and thus lowering the photocurrent.

J_{sc} remains relatively stable at lower defect densities but begins to decrease at Nt ≥ 10^{15} cm^{-3}, as carrier diffusion lengths become insufficient for effective charge extraction. The fill factor shows a nonlinear trend, initially stable but rapidly declining beyond the threshold defect density, indicating a transition from ideal to recombination-limited diode behavior. These results underscore the pivotal role of bulk defect passivation in perovskite absorber layers, where minimizing trap density below 5 × 10^{14} cm^{-3} is essential to preserving charge carrier lifetimes, maximizing voltage output, and maintaining overall power conversion efficiency. These trends highlight the fundamental limitation imposed by bulk traps on perovskite device efficiency and reinforce the critical need for high-quality film processing. Fig. 5(d) illustrates that the fill factor initially remains above 79%, even showing a slight rise from 10^{12} to 10^{14} cm^{-3}, likely due to improved diode quality in simulations. However, FF drops dramatically beyond 10^{15} cm^{-3}, falling below 70% at 10^{17} cm^{-3}. This reduction arises from distorted *J–V* characteristics, driven by trap-assisted recombination that reduces both the slope of the *I–V* curve near the maximum power point and increases the recombination tail in the forward bias regime.

In summary, the simulations demonstrate that bulk defect density is a critical parameter governing photovoltaic performance. To maintain high PCE, it is essential to suppress Nt to below 10^{14} cm^{-3}, ensuring long carrier lifetimes, efficient extraction, and minimal recombination losses. These insights reinforce the importance of high-quality crystallization, surface passivation, and defect-tolerant material engineering in perovskite solar cell fabrication.

Practical factors such as film non-uniformity, dopant instability in Spiro-OMeTAD (e.g., Li-TFSI/tBP), hygroscopic degradation, and interfacial corrosion are not neglected; rather, they are represented through their dominant electrical consequences. In drift–diffusion physics, such effects translate into reduced hole mobility and increased bulk/interface trap density, leading to enhanced SRH recombination. The systematic mobility and defect-density sensitivity analyses in Sections 3.3–3.7 show that efficiency collapses beyond bulk Nt ≈ 10^{15} cm^{-3} (Fig. 5) and interface Nt ≈ 5 × 10^{13} cm^{-2} (Fig. 8), indicating that the reported 21.45% PCE is a defect- and transport-constrained electronic upper

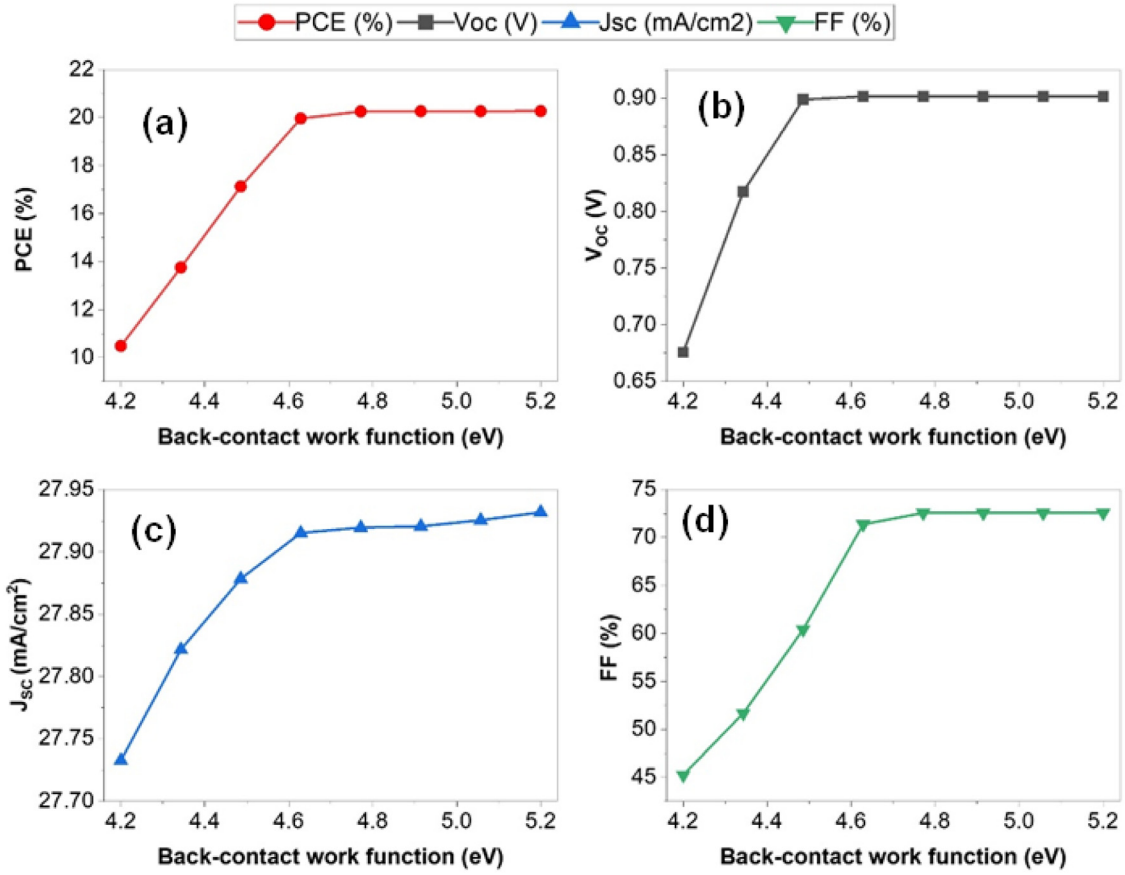

Fig. 6. Impact of back-contact work function (4.2–5.2 eV) on key photovoltaic parameters of a planar HTL-Polymer based PSC: (a) PCE, (b) V_{oc}, (c) J_{sc}, and (d) FF. Efficient hole extraction and minimized interfacial recombination are achieved when the back-contact work function aligns closely with the perovskite valence band.

bound rather than an assumption of ideal chemical or morphological stability.

3.5. Impact of rear-contact on the operational characteristics of polymer-HTL perovskite devices

Fig. 6 presents the impact of adjusting the back-contact work function between 4.2 and 5.2 eV on the main performance indicators of the HTL-based device. This study evaluates the impact on PCE (Fig. 6(a)), V_{oc} (Fig. 6(b)), J_{sc} (Fig. 6(c)), and fill factor (Fig. 5(d)). The back-contact work function significantly influences energy band alignment at the HTL/metal interface, directly affecting carrier extraction efficiency, interface recombination rates, and overall device performance [50]. Using the previously optimized HTL thickness (0.05 μm), absorber thickness (0.8 μm), and ETL doping (1×10^{18} cm^{-3} and thickness of 0.5 μm), the back-contact work function was varied while maintaining all other parameters constant.The PCE curve in Fig. 6(a) demonstrates a steep rise from approximately 12% at a work function of 4.2 eV to nearly 21% as the work function approaches 4.8 eV. This rapid increase can be attributed to enhanced band alignment at the back-contact interface, which minimizes carrier recombination and optimizes charge extraction. Beyond 4.8 eV, the PCE plateau suggests that the internal potential barrier becomes sufficiently aligned, resulting in diminished sensitivity to further increases in work function. This trend indicates that the optimal back-contact work function lies in the range of 4.8–5.0 eV, where the balance between charge extraction and interface recombination reaches its peak efficiency.

Fig. 6(b) reveals a steep rise in V_{oc}, increasing from roughly 0.7 V at 4.2 eV to nearly 0.9 V near 4.6 eV. This rapid improvement reflects reduced non-radiative recombination losses as the work function aligns more closely with the perovskite's conduction band, thereby minimizing the built-in field mismatch. The stabilization of V_{oc} beyond 4.6 eV indicates a The J_{sc} profile in Fig. 6(c) exhibits a more gradual increase, starting from approximately 27.7 mA/cm^2 at 4.2 eV and reaching a near-constant value of about 27.95 mA/cm^2 around 4.8 eV. This trend suggests that higher work functions facilitate improved charge separation and reduced recombination at the rear electrode, though the J_{sc} remains less sensitive to work function variations compared to V_{oc}, likely due to the stronger influence of bulk absorption and carrier diffusion length. point where the band offset is fully optimized, reducing further gain from work function adjustments. Similarly, the FF (Fig. 6(d)) increases significantly from around 50% at 4.2 eV to nearly 75% at 4.8 eV, reflecting improved device rectification and reduced series resistance, which collectively enhances overall device efficiency. These trends underscore the critical role of optimizing the back-contact work function to balance charge extraction and interface recombination, thereby achieving peak PCE in planar perovskite solar cells. From this analysis, the optimal back-contact work function is approximately 4.8 eV (Mo), where the device achieves peak PCE, stabilized V_{oc}, and maximum FF. Molybdenum provides excellent energy level alignment and superior electrical conductivity, promoting efficient charge extraction and reduced interface recombination.

3.6. Impact of operating temperature on the performance of HTL-polymer-based $CsSnI_2Br$ performance

Fig. 7 presents a comprehensive evaluation of the temperature dependence of key performance parameters in hole transport layer (HTL) polymer-based perovskite solar cells (PSCs), including power conversion efficiency (PCE), open-circuit voltage (V_{oc}), short-circuit current

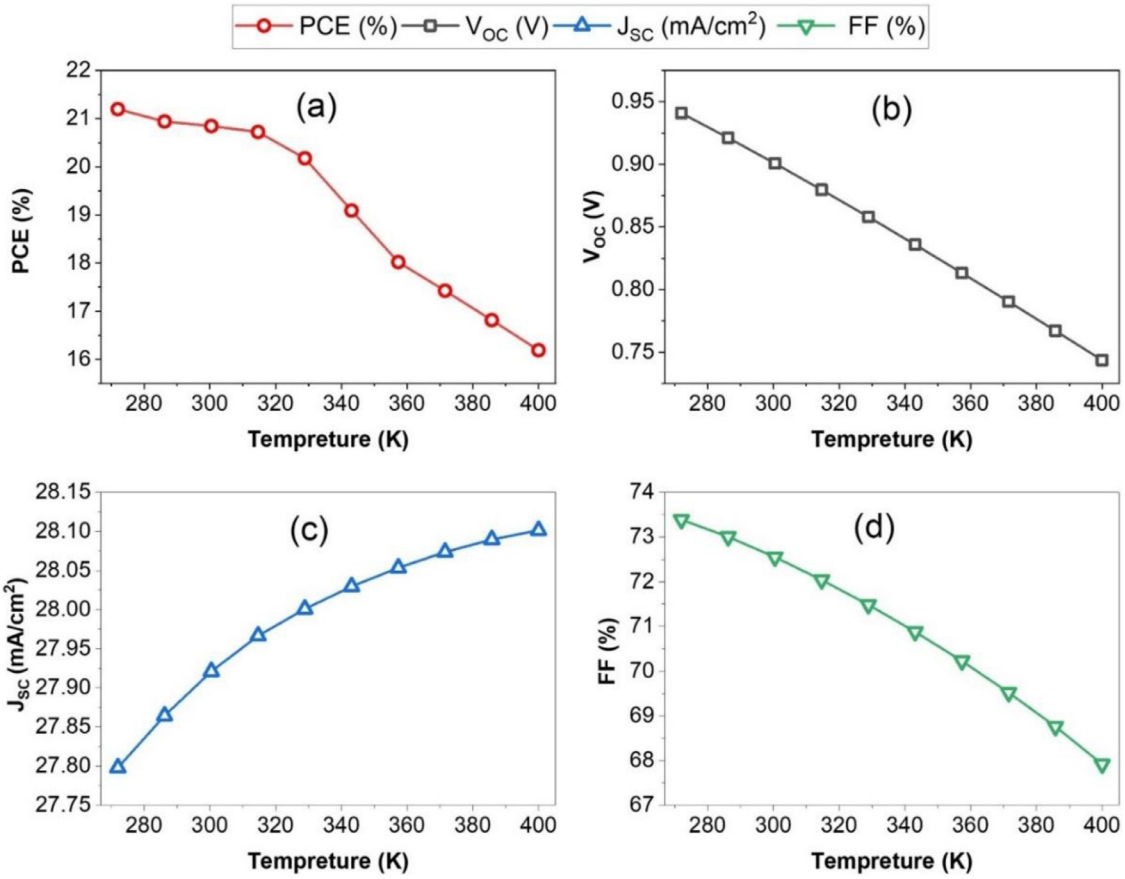

Fig. 7. Operating temperature-dependent performance analysis of HTL-polymer-based perovskite solar cells, showing the variation in (a) PCE, (b) V_{oc}, (c) J_{sc}, and (d) FF over a temperature range from 280 to 400 K.

density (J_{sc}), and fill factor (FF). These parameters are critical for understanding the thermal stability and operational limits of PSCs, which significantly influence their commercial viability. As shown in Fig. 7(a), the PCE exhibits a pronounced decline as the temperature increases from 280 to 400 K, decreasing from approximately 21% to 16%. This trend can be attributed to multiple thermal effects, including increased charge carrier recombination, enhanced ionic migration within the perovskite absorber, and the potential for thermal degradation at the HTL-polymer interface at higher temperatures.

Fig. 7(b) displays a near-linear drop in V_{oc}, shifting from about 0.95 V at 280 K to close to 0.75 V at 400 K. This trend is primarily driven by the exponential increase in reverse saturation current (J_0) with temperature, as described by Eq. (3):

$$J_0(T) = J_{00}T^3 \exp\left(-\frac{E_g}{kT}\right), \tag{3}$$

where J_{00} is a pre-factor, E_g is the bandgap energy, k is the Boltzmann constant, T and is the absolute temperature [51]. According to Shockley Eq. (1), this exponential dependence results in a sharp rise with temperature, resulting in a significant reduction in the quasi-Fermi level splitting and a direct decrease. As illustrated in Fig. 6(c), J_{sc} rises modestly from around 27.8 to approximately 28.2 mA/cm^2 as the temperature increases from 280 to 400 K, due to improved mobility and reduced recombination. However, this positive effect is often offset by more significant losses in and limiting the net impact on PCE.

The performance analysis presented in Fig. 7 indicates that HTL-polymer-based perovskite solar cells exhibit robust stability and high efficiency within a temperature range up to approximately 320 K (47 °C). In this range, the power conversion efficiency (PCE) remains above 20%, the open-circuit voltage (V_{oc}) is relatively stable, and the fill factor (FF) maintains high values, reflecting efficient charge extraction and reduced recombination losses. This favorable thermal stability is a promising characteristic for real-world photovoltaic applications, suggesting that these devices can sustain high performance under moderate thermal stress. However, maintaining temperatures within this range is essential to prevent the rapid efficiency losses observed at higher temperatures, emphasizing the importance of effective thermal management and interface engineering in device design. As a result of this favorable thermal stability, these devices are promising for real-world photovoltaic applications as they can maintain high performance under moderate thermal stress, providing a practical pathway for energy harvesting under varying environmental conditions in a stable and efficient manner. The temperature sweep reflects intrinsic electronic transport behavior under steady-state conditions and does not incorporate thermomechanical degradation, ion migration kinetics, or long-term chemical instability.

3.7. Impact of interface defects density on HTL-polymer based $CsSnI_2Br$ performance parameters

3.7.1. Impact of PEDOT:PSS/$CsSnI_2Br$ interface defects density on PV performance

The interface between the hole transport layer (HTL) and the absorber in PSC plays a critical role in determining overall device efficiency. Interface defects at (HTL/PSC) interface, often quantified as interfacial (IF) defect densities, significantly influence the charge extraction, recombination dynamics, and carrier transport properties of PSCs [52]. These defects can act as non-radiative recombination centers, increase leakage currents, and degrade all optoelectronic performance parameters. The simulations presented in this work were conducted by applying the interface (IF) defect densities summarized in Table 2. These

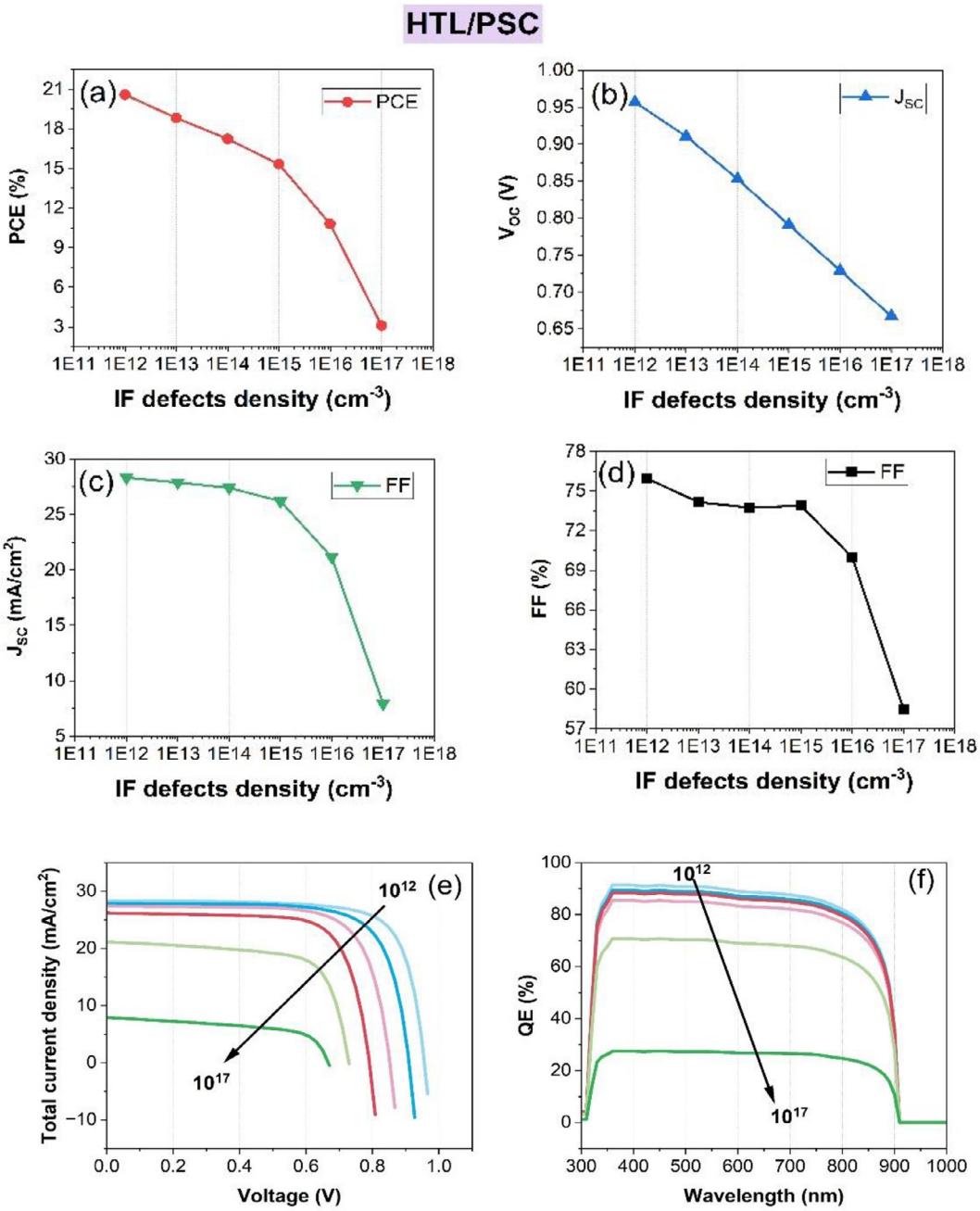

Fig. 8. Impact of HTL/PSC interface defect density on PSC performance. (a) PCE, (b) V_{oc}, (c) J_{sc}, (d) FF, (e) *J-V* curves, showing overall performance decline with increased IF defect density. (f) QE spectra, indicating reduced charge collection and increased recombination at higher IF defect densities.

defect parameters, including capture cross sections, defect energy levels, and total densities, were incorporated to accurately model the carrier recombination and charge transport behavior at both the HTL/PSC and PSC/ETL interfaces. This approach ensures a comprehensive understanding of the impact of defect density on device performance, providing critical insights for optimizing perovskite solar cell efficiency.

As depicted in Fig. 8(a), the device efficiency falls sharply, decreasing from just above 20% to nearly 2% when the defect density rises from the low-10^{12} range to the upper-10^{17} cm^{-3} regime. This loss in performance stems from increased nonradiative recombination at the HTL perovskite boundary. The behavior is governed by the Shockley–Read–Hall recombination model given below [43,53]:

$$R_{SRH} = \frac{np - n_i^2}{\tau_p(n + n_1) + \tau_n(p + p_1)}, \quad (4)$$

where R_{SRH} is the recombination rate, n and p are the electron and hole densities, n_i is the intrinsic carrier concentration, and τ_n and τ_p are the electron and hole lifetimes, respectively, which are inversely related to the defect density.

According to SRH recombination theory, an increase in defect density leads to a greater number of trap states within the material, significantly elevating recombination events. These trap states capture charge carriers, preventing efficient charge extraction to the electrodes. Consequently, increased defect densities escalate the recombination rate, thereby directly diminishing critical performance parameters, including the overall power conversion efficiency. V_{oc} is shown in Fig. 8(b) decreasing from 0.95 V to approximately 0.68 V with increasing defect density. In accordance with this trend, increased interface defects increase recombination losses, thus reducing the quasi-Fermi level splitting within the active perovskite layer, resulting in a reduction in V_{oc}.

The alignment of energy levels at the absorber/HTL interface plays a crucial role in determining the charge extraction efficiency and minimizing recombination losses in perovskite solar cells. A well-matched valence band offset facilitates efficient hole transfer from the absorber to the HTL while suppressing interfacial energy barriers. In this work, HTLs such as PTAA and Poly-TPD were selected due to their valence band positions closely aligned with that of $CsSnI_2Br$, enabling favorable band bending and reduced hole accumulation. This design guideline is consistent with recent findings indicating that proper alignment of energy levels at the perovskite and transport layer interface is crucial for improving carrier transport, minimizing loss mechanisms, and boosting the performance of tin-based, lead-free perovskite devices [54–56].

In Fig. 8(c), a significant reduction of J_{sc} from approximately 29 mA/cm^2 to less than 13 mA/cm^2 at higher defect densities (>5 × 10^{13} cm^{-3}) emphasizes the detrimental effect of IF defects on the effective carrier extraction. Increased defect density introduces additional trapping centers, lowering the charge carrier collection efficiency [54,55]. The relationship describing J_{sc} can be expressed as:

$$J_{SC} = q\int_0^d G(x)\mathrm{d}x - q\int_0^d R(x)\mathrm{d}x, \tag{5}$$

where $G(x)$ and $R(x)$ are the generation and recombination rates within the absorber layer [51]. A similar decline in FF is evident in Fig. 8(d), which indicates the pronounced impact of interface defects on the internal resistance and charge extraction mechanisms within the device. In addition to recombination losses, the fill factor is affected by series/shunt resistances, with higher defect densities exacerbating these losses, which are mathematically represented as follows:

$$FF = \frac{P_{Max}}{V_{oc} \times J_{sc}}, \tag{6}$$

where P_{Max} is the maximum power output under standard testing conditions (STC).

According to Figs. 8(e)(f), the external quantum efficiency (QE) and total current density-voltage characteristics are exhibited as a function of the IF defect density from 10^{12} to 10^{17} cm^{-3}, respectively. Fig. 7(e) demonstrates diminished photovoltaic behavior, which is characterized by a decreased slope and lowered J_{sc} and V_{oc} with increased defects, indicating a higher level of recombination and decreased charge collection efficiency [56]. As shown in Fig. 8(f), there is a significant reduction in QE with an increase in defect density, from nearly 90% to less than 30%. This observation supports the concept that an increase in defect density reduces charge collection and enhances recombination. These findings imply that higher defect densities in solar cells can lead to a substantial decrease in their efficiency. As defects increase, the ability of the solar cell to collect charge carriers diminishes, resulting in lower current output and reduced overall power conversion efficiency. Therefore, minimizing defect density is crucial for enhancing the performance and longevity of solar cells. In conclusion, the optimum interface (IF) defect density for maintaining robust photovoltaic performance in perovskite solar cells is approximately 5 × 10^{13} cm^{-3}. Under this defect level, the cell approaches peak operation, delivering an efficiency near 20.26%, a V_{oc} of roughly 0.92 volts, a J_{sc} close to 28.16 mA cm^{-2}, and a fill factor of about 75.48%. This level effectively balances minimal recombination losses with high overall device efficiency, as it significantly reduces the density of trap states that capture charge carriers, thereby enhancing charge collection at the electrodes. This balance is essential for sustaining high external quantum efficiency and maximizing overall power output, making it a crucial design parameter for optimizing device performance. This highlights the importance of controlling defect density during the fabrication process to optimize solar cell performance. Strategies such as improving material quality and employing advanced defect passivation techniques can help mitigate these effects.

3.7.2. Impact of $CsSnI_2Br/TiO_2$ interface defects density on PV performance

This section, as depicted in Fig. 9, illustrates the impact of interface defects density (IF) on photovoltaic device performance at the perovskite solar cell interface $CsSnI_2Br$ (PSC)/TiO_2(ETL). As a result of this study, a clear understanding of the impact of PSC/ETL IF defects density on critical performance parameters is obtained. Using the fully optimized device architecture, the HTL/perovskite and perovskite/ETL interface defect densities were independently varied to evaluate recombination-driven performance degradation. It is important to clarify that chemical instability of PEDOT:PSS (e.g., acidity-driven ITO corrosion or interfacial oxidation) is not ignored in this study; rather, it is represented through its dominant device-level electrical consequence: increased interface trap density. In continuum drift–diffusion modeling, electrochemical degradation manifests physically as elevated interface recombination velocity and trap-assisted Shockley–Read–Hall (SRH) recombination. The interface defect formalism defined in Table 2 (variable Nt, capture cross-sections, and trap energetics) provides a physically consistent framework to emulate corrosion-induced interfacial deterioration. As demonstrated in Fig. 8, increasing the HTL/$CsSnI_2Br$ interface defect density beyond ~5 × 10^{13} cm^{-2} causes a pronounced suppression of V_{oc} and FF due to enhanced SRH recombination (Eq. (4)). Therefore, any corrosion-driven interface degradation in PEDOT: PSS is quantitatively captured in this model through elevated Nt, which directly reduces carrier lifetime and diffusion length ($L = \sqrt{D\tau}$). This confirms that the predicted 21.45% efficiency is attainable only under controlled interface quality, and that chemical instability would immediately shift the device into the recombination-limited regime identified in this work.

Therefore, reducing the interface defect density can lead to significant improvements in photovoltaic performance. By optimizing the interface quality, charge carrier recombination can be minimized, resulting in higher power conversion efficiency. In addition, enhancing the stability of the interface can enhance the long-term reliability of perovskites solar cells. Similar trend as observed at HTL/PSC interface Fig. 9(a) shows that increasing the IF defect density drastically reduces the PCE from approximately 21% at a defect density of 10^{12} cm^{-3} down to nearly 2% at 10^{17} cm^{-3}. This severe performance degradation primarily results from increased trap-assisted recombination, diminishing the effective collection of photogenerated carriers. This behavior is quantitatively described by the Shockley-Read-Hall (SRH) (Eq. (4)). Fig. 8(b) reveals a steady decrease in V_{oc} from approximately 0.98 to around 0.83 V with rising IF defects. This trend is closely related to the increase in recombination activities, as described by the Shockley Diode law (Eq. (1)) under open-circuit conditions [57].

In Fig. 9(d), FF remains around 80% at lower defect densities and drops to 69% after 10^{15} cm^{-3}. Increased recombination and resistance losses at the PSC/ETL interface are responsible for the degradation of FF at elevated defect densities. In non-radiative recombination, charge carriers recombine without emitting photons, thus losing energy as heat. The number of charge carriers available for extraction is reduced due to this process, which reduces the overall efficiency of the device. In turn, this negatively affects the efficiency of power conversion by lowering J_{sc} and FF metrics Figs. 9(c)(d) [44,58].

The *J-V* curves clearly illustrate the detrimental impact of higher defect densities (Fig. 9(f)). The devices with lower defect densities (<10^{14} cm^{-3}) maintain superior current density and higher open-circuit voltage, while those with higher defect densities exhibit significantly compressed J-V curves, confirming substantial recombination losses. External quantum efficiency (QE) decreases significantly as defect density increases (Fig. 8(e)). At lower defect densities (~10^{14} cm^{-3}), the QE remains high across the entire visible spectrum, indicating efficient photogenerated carrier extraction [59]. However, as the defect density reaches 10^{17} cm^{-3}, the QE drops dramatically, reflecting severe recombination losses and reduced carrier mobility. To maintain robust photovoltaic performance, the optimal IF defect density should remain be-

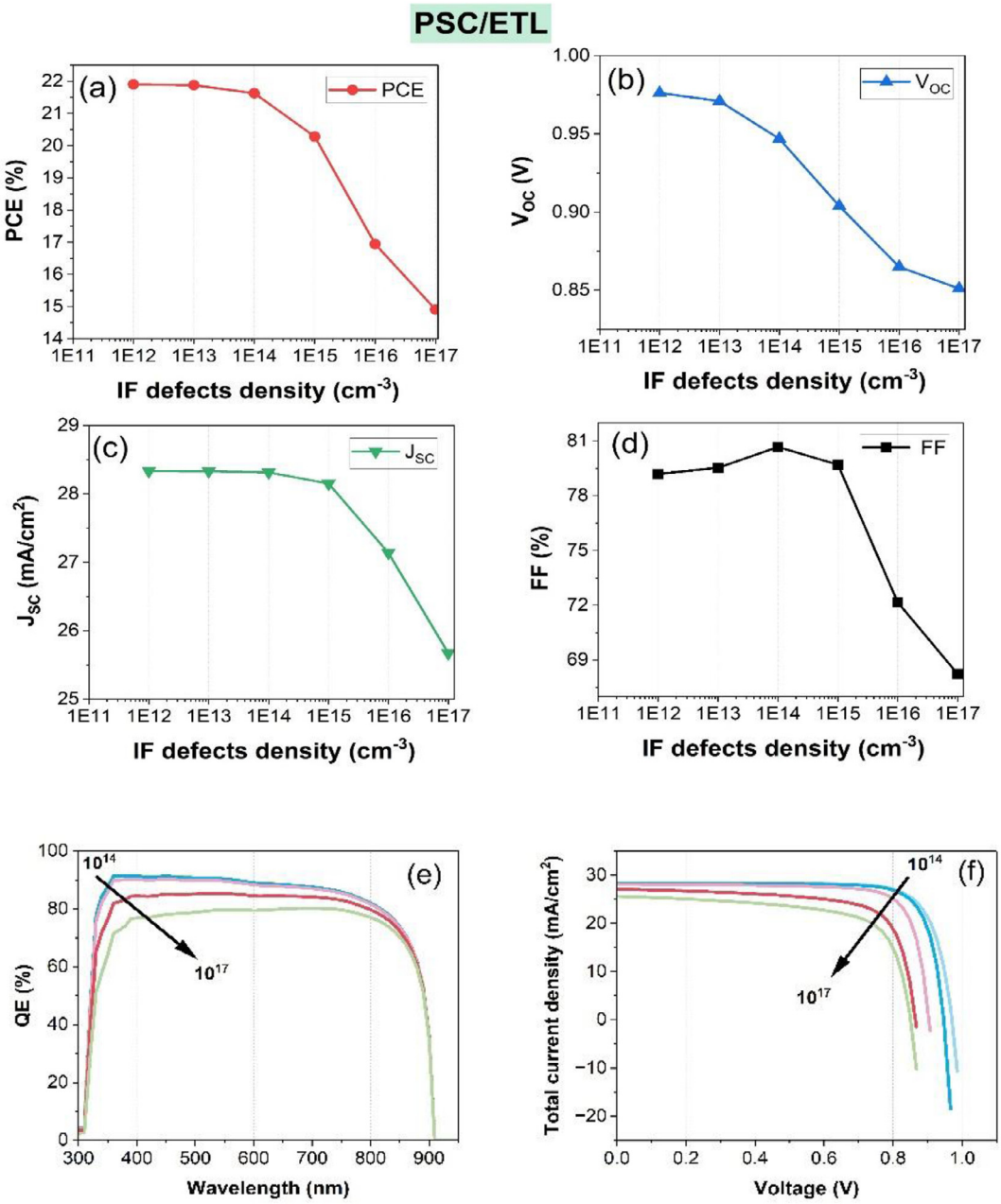

Fig. 9. Impact of PSC/ETL interface defect density on PSC performance. (a) PCE, (b) V_{oc}, (c) J_{sc}, (d) FF, (e) *J-V* curves, showing overall performance decline with increased IF defect density. (f) QE spectra, indicating reduced charge collection and increased recombination at higher IF densities.

low 10^{15} cm^{-3}. At this level, the device achieves near-maximum PCE (~21.26%), high open-circuit voltage (V_{oc} around 0.95–0.98 V), substantial short-circuit current density (J_{sc} around 28 mA/cm^2), and excellent fill factor (FF ~80%–81%). This defect range effectively minimizes non-radiative recombination losses, ensuring efficient carrier extraction and superior overall device efficiency.

Table 3 presents a comparative analysis of the photovoltaic performance of our optimized $CsSnI_2Br$-based solar cell in relation to recent state-of-the-art experimental and simulated studies. Our device architecture achieves a simulated power conversion efficiency (PCE) of 21.45%, with an open-circuit voltage (V_{oc}) of 0.97 V, a short-circuit current density (J_{sc}) of 28.65 mA/cm^2, and a fill factor (FF) of 77.2%. These values

Table 3
Comparative performance of simulated $CsSnI_2Br$-based and experimental $CsSnI_{3-x}Br_x$-based perovskite solar cells.

Absorber Material	PCE (%)	V_{oc} (V)	J_{sc} (mA/cm^2)	FF (%)	Remarks	Ref.
$CsSnI_2Br$	21.45 (simulated)	0.97	28.65	77.2	HTL optimization; defect & thermal analysis	This Work
$CsSnI_{3-x}Br_x$	19.76 (simulated)	0.94	27.80	76.1	Bandgap grading and material design	[60]
$CsSnI_3$ + CNT-TSC	23.34 (experimental)	0.91	28.70	80.3	Defect passivation using CNT-TSC	[61]
$CsSnI_{3-x}Br_x$ (tri-layer)	20.54 (simulated)	0.95	26.45	81.0	ETL/absorber interface tuning	[62]
$CsSnI_3$	11.9 (experimental)	0.83	23.9	61.9	Lattice strain impact on Sn-based PSC	[63]

reflect a substantial performance enhancement compared to previously reported $CsSnI_{3-x}Br_x$-based devices. For instance, Kaur et al. [60] reported a simulated PCE of 19.76% via bandgap grading of $CsSnI_{3-x}Br_x$, while Dar and Sengar [62] achieved 20.54% using a tri-layer heterojunction structure. The highest experimental efficiency in the comparison (23.34%) was reported by Alshaeer et al. [61], who utilized carbon nanotube-assisted defect passivation, though with a lower V_{oc} of 0.91 V. In contrast, Nishimura et al. [63] achieved only 11.9% experimentally for unmodified $CsSnI_3$, highlighting the limitations of untreated tin-based perovskites.

The superior performance of our device is attributed to the combined optimization of polymeric HTLs, interfacial defect suppression, and back-contact energetics. This study, therefore, demonstrates the critical importance of holistic interface engineering strategies in unlocking the full potential of $CsSnI_2Br$ as a lead-free absorber for next-generation perovskite photovoltaics

4. Conclusions

This study evaluated the performance optimization of $CsSnI_2Br$ perovskite solar cells using an advanced numerical model based on SCAPS-1D. Based on the findings, it is evident that the choice of the hole transport layer, the absorber thickness, and the doping of the electron transport layer have a significant impact on the device's efficiency and stability. PEDOT:PSS achieved superior performance compared to the other polymer-based HTLs due to its favorable energy level alignment and efficient hole extraction, establishing it as a top candidate for high-efficiency PSCs. Optimal device performance was achieved by balancing the absorber and HTL thicknesses in a way that reduced resistive losses and enhanced charge transport, while retaining interfacial stability. Additionally, optimizing ETL thickness and doping concentration significantly enhanced electron extraction and minimized series resistance, further improving overall power conversion efficiency. Moreover, this study emphasizes the importance of defect management, as low defect densities are shown to significantly improve photovoltaic performance by reducing non-radiative recombination and improving operational stability. The device was also thermally stable up to 320 K, which was quite impressive for a thin architecture. Collectively, these findings provide crucial insights into the design of lead-free perovskite solar technologies, supporting their continued development towards scalable, commercially viable, and environmentally sustainable photovoltaic solutions.

Declaration of Competing Interest

The authors declare that they have no known competing financial interests or personal relationships that could have appeared to influence the work reported in this paper.

CRediT authorship contribution statement

Wasan J. Kadhem: Writing – review & editing, Writing – original draft, Visualization, Validation, Software, Resources, Methodology, Investigation, Formal analysis, Data curation, Conceptualization. **Tariq AlZoubi:** Writing – review & editing, Writing – original draft, Visualization, Validation, Supervision, Software, Resources, Project administration, Methodology, Investigation, Funding acquisition, Formal analysis, Data curation, Conceptualization. **Mahmoud AlGharram:** Writing – review & editing, Visualization, Validation, Methodology, Formal analysis, Data curation. **Ghaseb Makhadmeh:** Writing – original draft, Validation, Resources, Formal analysis, Data curation. **Abdulsalam Abuelsamen:** Formal analysis, Data curation. **Ahmad M. AL-Diabat:** Validation, Data curation. **Jestin Mandumpal:** Funding acquisition, Formal analysis. **Samer H. Zyoud:** Formal analysis.

References

[1] F. Zhang, Z. Ma, Z. Shi, X. Chen, D. Wu, X. Li, C. Shan, Recent advances and opportunities of lead-free perovskite nanocrystal for optoelectronic application, Energy Mater. Adv. 2021 (2021) 5198145, doi:10.34133/2021/5198145.

[2] M. Di Sabatino, R. Hendawi, A.S. Garcia, Silicon solar cells: Trends, manufacturing challenges, and AI perspectives, Crystals 14 (2024) 167, doi:10.3390/cryst14020167.

[3] T. Al Zoubi, A. Moghrabi, M. Moustafa, S. Yasin, Efficiency boost of CZTS solar cells based on double-absorber architecture: Device modeling and analysis, Sol. Energy 225 (2021) 44–52, doi:10.1016/j.solener.2021.07.012.

[4] L. Huang, W.R.L. Lambrecht, Electronic band structure, phonons, and exciton binding energies of halide perovskites $CsSnCl_3$, $CsSnBr_3$, and $CsSnI_3$, Phys. Rev. B 88 (2013) 165203, doi:10.1103/PhysRevB.88.165203.

[5] P. Zhao, J. Su, Z. Lin, J. Wang, J. Zhang, Y. Hao, X. Ouyang, J. Chang, All-inorganic $CsPbI_xBr_{3-x}$ perovskite solar cells: Crystal anisotropy effect, Adv. Theory Simul. 3 (2020) 2000055, doi:10.1002/adts.202000055.

[6] J. Deng, J. Li, Z. Yang, M. Wang, All-inorganic lead halide perovskites: A promising choice for photovoltaics and detectors, J. Mater. Chem. C 7 (2019) 12415–12440, doi:10.1039/C9TC04164H.

[7] M. Shakil, A. Akram, I. Zeba, R. Ahmad, S.S.A. Gillani, M.A. Gadhi, Effect of mixed halide contents on structural, electronic, optical and elastic properties of $CsSnI_{3-x}Br_x$ for solar cell applications: First-principles study, Mater. Res. Express 7 (2020) 025513, doi:10.1088/2053-1591/ab727d.

[8] R. Padmavathy, A. Amudhavalli, R. Rajeswarapalanichamy, K. Iyakutti, Electronic structure and optical properties of $CsSnI_{3-y}Br_y$ ($y = 0, 1, 2, 3$) perovskites, Int. J. Mod. Phys. B 33 (2019) 1950003, doi:10.1142/S0217979219500036.

[9] B. Nakamanya, N. Yu, T. Kakooza, Q. Sun, A. Balilonda, S. Yang, M. Zhu, Stability and performance improvement of cesium tin halide perovskites with astaxanthin treatment, J. Mater. Chem. C 13 (2025) 5209–5220, doi:10.1039/D4TC04420G.

[10] B. Wu, Y. Zhou, G. Xing, Q. Xu, H.F. Garces, A. Solanki, T.W. Goh, N.P. Padture, T.C. Sum, Long minority-carrier diffusion length and low surface-recombination velocity in inorganic lead-free $CsSnI_3$ perovskite crystal for solar cells, Adv. Funct. Mater. 27 (2017) 1604818, doi:10.1002/adfm.201604818.

[11] M. Saliba, T. Matsui, J.Y. Seo, K. Domanski, J.P. Correa-Baena, M.K. Nazeeruddin, S.M. Zakeeruddin, W. Tress, A. Abate, A. Hagfeldt, M. Grätzel, Cesium-containing triple cation perovskite solar cells: Improved stability, reproducibility and high efficiency, Energy Environ. Sci. 9 (2016) 1989–1997, doi:10.1039/C5EE03874J.

[12] Q. Wang, A. Abate, Strategies toward stable perovskite solar cells, Adv. Mater. Interfaces 5 (2018) 1800264, doi:10.1002/admi.201800264.

[13] M.H. Li, X. Ma, J. Fu, S. Wang, J. Wu, R. Long, J.S. Hu, Molecularly tailored perovskite/poly(3-hexylthiophene) interfaces for high-performance solar cells, Energy Environ. Sci. 17 (2024) 5513–5520, doi:10.1039/d4ee02251c.

[14] Md.A. Karim, K. Matsuishi, Md.E. Kayesh, Y. He, A. Islam, Inhibition of Sn^{2+} oxidation in $FASnI_3$ perovskite precursor solution and enhanced stability of perovskite solar cells by reductive additive, ACS Appl. Mater. Interfaces 15 (2023) 45823–45833, doi:10.1021/acsami.3c07903.

[15] R. Zhao, N. Wang, Y. Yu, J. Liu, Organoboron polymer for 10% efficiency all-polymer solar cells, Chem. Mater. 32 (2020) 1308–1314, doi:10.1021/acs.chemmater.9b04997.

[16] S.A. Dar, B.S. Sengar, Design and performance optimization of a novel tri-layer unleaded all inorganic lead-free mixed halide $CsSnI_{3-x}Br_x$ heterojunction solar cell, Sol. Energy 275 (2024) 112618, doi:10.1016/j.solener.2024.112618.

[17] N.D. Davlatshoevich, Investigation optical properties of the orthorhombic system $CsSnBr_{3-x}I_x$: Application for solar cells and optoelectronic devices, J. Hum. Earth Future 2 (2021) 404–411, doi:10.28991/HEF-2021-02-04-08.

[18] D.S. Thakur, R.K. Sharma, V. Garg, S. Yadav, DFT-based accurate and efficient bandgap prediction of $CsSnI_{3-x}Br_x$ and parameter optimization for enhanced perovskite solar cell performance, Phys. B 697 (2025) 416693, doi:10.1016/j.physb.2024.416693.

[19] M.H. Li, F.Z. Qiu, S. Wang, Y. Jiang, J.S. Hu, Hole transporting materials in inorganic $CsPbI_{3-x}Br_x$ solar cells: Fundamentals, criteria and opportunities, Mater. Today 52 (2022) 250–268, doi:10.1016/j.mattod.2021.11.017.

[20] N. Kaur, J. Madan, R. Pandey, Maximizing photovoltaic performance of all-inorganic perovskite $CsSnI_{3-x}Br_x$ solar cells through bandgap grading and material design, Sol. Energy 274 (2024) 112573, doi:10.1016/j.solener.2024.112573.

[21] D.D. Nematov, A.S. Burhonzoda, M.A. Khusenov, Kh.T. Kholmurodov, T. Yamamoto, First principles analysis of crystal structure, electronic and optical properties of $CsSnI_{3-x}Br_x$ perovskite for photoelectric applications, J. Surf. Investig. X-ray Synchrotron Neutron Tech. 15 (2021) 532–536, doi:10.1134/S1027451021030149.

[22] F. Alshaeer, M.A. Mohammed, M. Zorah, N. Alharbi, H.M.A. Mahmoud, A.M.E. Ahmed, B.A. Mohammed, G. Abdulkareem-Alsultan, M.F. Nassar, Synergistic defect passivation and charge transport enhancement via thiosemicarbazide-functionalized carbon nanotubes for high-efficiency lead-free $CsSnI_3$ perovskite solar cells: A pathway to 23.34% efficiency, J. Alloys Compd. 1026 (2025) 180428, doi:10.1016/j.jallcom.2025.180428.

[23] J. Liu, S. Wang, W. Zhu, Z. Tang, L. Ding, F. Hao, Highly symmetric Lewis base coordinated with Sn^{2+} for reducing voltage loss and retarding oxidation in tin-halide perovskite solar cells, Chem. Eng. J. 453 (2023) 139975, doi:10.1016/j.cej.2022.139975.

[24] D. Jones, Y. An, J. Hidalgo, C. Evans, J.N. Vagott, J.P. Correa-Baena, Polymers and interfacial modifiers for durable perovskite solar cells: A review, J. Mater. Chem. C 9 (2021) 12509–12522, doi:10.1039/D1TC01243F.

[25] Y. Ma, J. Ge, A.K.Y. Jen, J. You, S. Liu, Polymer boosts high performance perovskite solar cells: A review, Adv. Opt. Mater. 12 (2024) 2301623, doi:10.1002/adom.202301623.

[26] J. Bing, J. Kim, M. Zhang, J. Zheng, D.S. Lee, Y. Cho, X. Deng, C.F.J. Lau, Y. Li, M.A. Green, S. Huang, A.W.Y. Ho-Baillie, The impact of a dynamic two-step solution process on film formation of $Cs_{0.15}(MA_{0.7}FA_{0.3})_{0.85}PbI_3$ perovskite and solar cell performance, Small 15 (2019) 1804858, doi:10.1002/smll.201804858.

[27] D.J. Fairfield, H. Sai, A. Narayanan, J.V. Passarelli, M. Chen, J. Palasz, L.C. Palmer, M.R. Wasielewski, S.I. Stupp, Structure and chemical stability in perovskite–polymer hybrid photovoltaic materials, J. Mater. Chem. A 7 (2019) 1687–1699, doi:10.1039/C8TA07545J.

[28] S. Wang, X.Y. Gong, M.X. Li, M.H. Li, J.S. Hu, Polymers for perovskite solar cells, JACS Au 4 (2024) 3400–3412, doi:10.1021/jacsau.4c00615.

[29] S. Wang, H. Yao, W. Zhu, C. Wu, Z. Tang, J. Liu, L. Ding, F. Hao, Stabilization of perovskite lattice and suppression of Sn^{2+}/Sn^{4+} oxidation via formamidine acetate for high efficiency tin perovskite solar cells, Adv. Funct. Mater. 33 (2023) 2215041, doi:10.1002/adfm.202215041.

[30] L. Chen, H. Cai, X. Luo, X. Zhao, S. Wu, Modifying the buried PEDOT:PSS/perovskite interface by dual-functional material to optimize the performance of pure Sn-based perovskite solar cells, Surf. Interfaces 57 (2025) 105743, doi:10.1016/j.surfin.2025.105743.

[31] M.T. Dang, L. Hirsch, G. Wantz, P3HT:PCBM, best seller in polymer photovoltaic research, Adv. Mater. 23 (2011) 3597–3602, doi:10.1002/adma.201100792.

[32] M.H. Li, X. Gong, S. Wang, L. Li, J. Fu, J. Wu, Z.A. Tan, J.S. Hu, Facile hydrogen-bonding assisted crystallization modulation for large-area high-quality $CsPbI_2Br$ films and efficient solar cells, Angew. Chem. Int. Ed. 136 (2024) e202318591, doi:10.1002/anie.202318591.

[33] M. Burgelman, P. Nollet, S. Degrave, Modelling polycrystalline semiconductor solar cells, Thin Solid Films 361–362 (2000) 527–532, doi:10.1016/S0040-6090(99)00825-1.

[34] M. Burgelman, K. Decock, S. Khelifi, A. Abass, Advanced electrical simulation of thin film solar cells, Thin Solid Films 535 (2013) 296–301, doi:10.1016/j.tsf.2012.10.032.

[35] T. Al Zoubi, B. Mourched, M. Al Gharram, G. Makhadmeh, O.Abu Noqta, Improving photovoltaic performance of hybrid organic-inorganic $MAGeI_3$ perovskite solar cells via numerical optimization of carrier transport materials (HTLs/ETLs), Nanomaterials 13 (2023) 2221, doi:10.3390/nano13152221.

[36] M. Moustafa, T. Al Zoubi, S. Yasin, Numerical analysis of the role of p-$MoSe_2$ interfacial layer in CZTSe thin-film solar cells using SCAPS simulation, Optik 247 (2021) 167885, doi:10.1016/j.ijleo.2021.167885.

[37] S. Yasin, Z.A. Waar, T. Al Zoubi, M. Moustafa, High efficiency performance of eco-friendly $C_2N/FASnI_3$ double-absorber solar cell probed by numerical analysis, Opt. Mater. 122 (2021) 111743, doi:10.1016/j.optmat.2021.111743.

[38] S. Yasin, Z.A. Waar, T. Al Zoubi, M. Moustafa, Optoelectronic simulation of a high efficiency C_2N based solar cell via buffer layer optimization, Opt. Mater. 119 (2021) 111364, doi:10.1016/j.optmat.2021.111364.

[39] M. Moustafa, T. Alzoubi, Numerical study of CdTe solar cells with p-$MoTe_2$ TMDC as an interfacial layer using SCAPS, Mod. Phys. Lett. B 32 (2018) 1850269, doi:10.1142/S021798491850269X.

[40] M. Moustafa, T. Al Zoubi, S. Yasin, Optoelectronics simulation of CIGS-based solar cells using a Cd-free nontoxic ZrS_xSe_{2-x} as a novel buffer layer, Braz. J. Phys. 52 (2022) 1–10, doi:10.1007/s13538-022-01146-z.

[41] T. Al Zoubi, M. Al-Gharram, M. Moustafa, Insights into the impact of defect states and temperature on the performance of kesterite-based thin-film solar cells, Optik 264 (2022) 169442, doi:10.1016/j.ijleo.2022.169442.

[42] M. Benyoucef, T. Alzoubi, J.P. Reithmaier, M. Wu, A. Trampert, Nanostructured hybrid material based on highly mismatched III–V nanocrystals fully embedded in silicon, Phys. Status Solidi A 211 (2014) 817–822, doi:10.1002/pssa.201330395.

[43] T. Al Zoubi, W.J. Kadhem, M. Al Gharram, G. Makhadmeh, M.A.O. Abdelfattah, A. Abuelsamen, A.M. AL-Diabat, O. Abu Noqta, B. Lazarevic, S.H. Zyoud, B. Mourched, Advanced optoelectronic modeling and optimization of HTL-free $FASnI_3$/C60 perovskite solar cell architecture for superior performance, Nanomaterials 14 (2024) 1062, doi:10.3390/nano14121062.

[44] S. Li, Y.L. Cao, W.H. Li, Z.S. Bo, A brief review of hole transporting materials commonly used in perovskite solar cells, Rare Met. 40 (2021) 2712–2729, doi:10.1007/s12598-020-01691-z.

[45] R. Sen, M. Yadav, An investigation on organic and inorganic materials for hole transport layer in lead-free third-generation solar cell, J. Opt. 52 (2023) 672–682, doi:10.1007/s12596-022-01027-3.

[46] Y. Wang, L. Duan, M. Zhang, Z. Hameiri, X. Liu, Y. Bai, X. Hao, PTAA as efficient hole transport materials in perovskite solar cells: A review, Sol. RRL 6 (2022) 2200234, doi:10.1002/solr.202200234.

[47] N. Rono, A.E. Merad, J.K. Kibet, B.S. Martincigh, V.O. Nyamori, Optimization of hole transport layer materials for a lead-free perovskite solar cell based on formamidinium tin iodide, Energy Technol. 9 (2021) 2100859, doi:10.1002/ente.202100859.

[48] Q.Y. Chang, Y.D. An, H.M. Cao, Y.Z. Pan, L.Y. Zhao, Y.L. Chen, Y. We, S.W. Tsang, H.L. Yip, L.C. Sun, Z. Yu, Precursor engineering enables high-performance all-inorganic $CsPbIBr_2$ perovskite solar cells with a record efficiency approaching 13%, J. Energy Chem. 90 (2024) 16–22, doi:10.1016/j.jechem.2023.10.021.

[49] A.S. Chouhan, N.P. Jasti, S. Avasthi, Effect of interface defect density on performance of perovskite solar cell: Correlation of simulation and experiment, Mater. Lett. 221 (2018) 150–153, doi:10.1016/j.matlet.2018.03.095.

[50] R. Ma, J. Yu, T. Liu, G. Zhang, Y. Xiao, Z. Luo, G. Chai, Y. Chen, Q. Fan, W. Su, G. Li, E. Wang, X. Lu, F. Gao, H. Yan, B. Tang, All-polymer solar cells with over 16% efficiency and enhanced stability enabled by compatible solvent and polymer additives, Aggregate 3 (2022) e58, doi:10.1002/agt2.58.

[51] H. Zhang, X. Qiao, Y. Shen, M. Wang, Effect of temperature on the efficiency of organometallic perovskite solar cells, J. Energy Chem. 24 (2015) 729–735, doi:10.1016/j.jechem.2015.10.007.

[52] G. Zhang, L. Wang, C. Zhao, Y. Wang, R. Hu, J. Che, S. He, W. Chen, L. Cao, Z. Luo, M. Qiu, S. Li, G. Zhang, Efficient all-polymer solar cells enabled by interface engineering, Polymers 14 (2022) 3835, doi:10.3390/polym14183835.

[53] V. Srivastava, S.H. Reddy, B. Anitha, A.G.M. Namboothiry, A comparative study of defect density of states for single, mixed and bulk heterojunction perovskite solar cells, AIP Conf. Proc. 2082 (2019) 050013, doi:10.1063/1.5093873.

[54] N.A. Tukadiya, Z.D. Ponkiya, N. Joshi, D. Upadhyay, P.K. Jha, Machine learning and SCAPS-1D based prediction and validation of $RbGeBr_3$ perovskite solar cell, Sol. Energy 300 (2025) 113760, doi:10.1016/j.solener.2025.113760.

[55] G. Pindolia, S.M. Shinde, P.K. Jha, Non-leaded, $KSnI_3$ based perovskite solar cell: A DFT study along with SCAPS simulation, Mater. Chem. Phys. 297 (2023) 127426, doi:10.1016/j.matchemphys.2023.127426.

[56] M. Benyoucef, M. Usman, T. Alzoubi, J.P. Reithmaier, Pre-patterned silicon substrates for the growth of III–V nanostructures, Phys. Status Solidi A 209 (2012) 2402–2410, doi:10.1002/pssa.201228367.

[57] T. Al Zoubi, M. Al-Gharram, G. Makhadmeh, O.Abu Noqta, Comparative analysis of optoelectronic and structural characteristics in electrochemically synthesized hybrid-nanocomposites based on PANI-CSA/metal oxide nanoparticles, Phys. B 713 (2025) 417380, doi:10.1016/j.physb.2025.417380.

[58] V.H. Diniz Araújo, A.F. Nogueira, J.C. Tristão, L.J. dos Santos, Fullerene-C60 and PCBM as interlayers in regular and inverted lead-free PSCs using $CH_3NH_3SnI_3$: An analysis of device performance and defect density dependence by SCAPS-1D, RSC Adv. 14 (2024) 10930–10941, doi:10.1039/D4RA00634H.

[59] I.M. Dharmadasa, J.D. Bunning, A.P. Samantilleke, T. Shen, Effects of multi-defects at metal/semiconductor interfaces on electrical properties and their influence on stability and lifetime of thin film solar cells, Sol. Energy Mater. Sol. Cells 86 (2005) 373–384, doi:10.1016/j.solmat.2004.08.009.

[60] X. Chen, J. Cheng, L. He, L. Zhao, C. Zhang, A. Pang, J. Li, Hole transport materials for tin-based perovskite solar cells: Properties, progress, prospects, Molecules 28 (2023) 3787, doi:10.3390/molecules28093787.

[61] C.H. Kuan, G.S. Luo, S. Narra, S. Maity, H. Hiramatsu, Y.W. Tsai, J.M. Lin, C.H. Hou, J.J. Shyue, E.W.G. Diau, How can a hydrophobic polymer PTAA serve as a hole-transport layer for an inverted tin perovskite solar cell? Chem. Eng. J. 450 (2022) 138037, doi:10.1016/j.cej.2022.138037.

[62] S.W. Park, J.H. Heo, H.J. Lee, H. Kim, S. Kim, S.H. Im, Compositional design for high-efficiency all-inorganic tin halide perovskite solar cells, ACS Energy Lett. 8 (2023) 5061–5069, doi:10.1021/acsenergylett.3c02032.

[63] K. Nishimura, D. Hirotani, M.A. Kamarudin, Q. Shen, T. Toyoda, S. Iikubo, T. Minemoto, K. Yoshino, S. Hayase, Relationship between lattice strain and efficiency for Sn-perovskite solar cells, ACS Appl. Mater. Interfaces 11 (2019) 31105–31110, doi:10.1021/acsami.9b09564.